View metadata, citation and similar papers at core.ac.uk

brought to you by CORE

provided by Scholarship at UWindsor

University of Windsor

Scholarship at UWindsor

Electronic Theses and Dissertations

Theses, Dissertations, and Major Papers

1-1-2006

A MEMS sonoluminescent ultrasonic sensor.

Andrew Tam
University of Windsor

Follow this and additional works at: https://scholar.uwindsor.ca/etd

Recommended Citation

Tam, Andrew, "A MEMS sonoluminescent ultrasonic sensor." (2006). *Electronic Theses and Dissertations*. 7057.
https://scholar.uwindsor.ca/etd/7057

This online database contains the full-text of PhD dissertations and Masters' theses of University of Windsor students from 1954 forward. These documents are made available for personal study and research purposes only, in accordance with the Canadian Copyright Act and the Creative Commons license—CC BY-NC-ND (Attribution, Non-Commercial, No Derivative Works). Under this license, works must always be attributed to the copyright holder (original author), cannot be used for any commercial purposes, and may not be altered. Any other use would require the permission of the copyright holder. Students may inquire about withdrawing their dissertation and/or thesis from this database. For additional inquiries, please contact the repository administrator via email (scholarship@uwindsor.ca) or by telephone at 519-253-3000ext. 3208.

A MEMS Sonoluminescent Ultrasonic Sensor

by

Andrew Tam

A Thesis
Submitted to the Faculty of Graduate Studies and Research
Through the Department of Electrical and Computer Engineering
in Partial Fulfillment of the Requirements for
the Degree of Master of Applied Science at the
University of Windsor

Windsor, Ontario, Canada

2006

©

2006 Andrew Tam

Reproduced with permission of the copyright owner. Further reproduction prohibited without permission.

Library and Archives Canada

Published Heritage Branch

395 Wellington Street
Ottawa ON K1A 0N4
Canada

Bibliothèque et Archives Canada

Direction du Patrimoine de l'édition

395, rue Wellington
Ottawa ON K1A 0N4
Canada

Your file Votre référence
ISBN: 978-0-494-35918-1
Our file Notre référence
ISBN: 978-0-494-35918-1

NOTICE:
The author has granted a non-exclusive license allowing Library and Archives Canada to reproduce, publish, archive, preserve, conserve, communicate to the public by telecommunication or on the Internet, loan, distribute and sell theses worldwide, for commercial or non-commercial purposes, in microform, paper, electronic and/or any other formats.

The author retains copyright ownership and moral rights in this thesis. Neither the thesis nor substantial extracts from it may be printed or otherwise reproduced without the author's permission.

AVIS:
L'auteur a accordé une licence non exclusive permettant à la Bibliothèque et Archives Canada de reproduire, publier, archiver, sauvegarder, conserver, transmettre au public par télécommunication ou par l'Internet, prêter, distribuer et vendre des thèses partout dans le monde, à des fins commerciales ou autres, sur support microforme, papier, électronique et/ou autres formats.

L'auteur conserve la propriété du droit d'auteur et des droits moraux qui protège cette thèse. Ni la thèse ni des extraits substantiels de celle-ci ne doivent être imprimés ou autrement reproduits sans son autorisation.

In compliance with the Canadian Privacy Act some supporting forms may have been removed from this thesis.

While these forms may be included in the document page count, their removal does not represent any loss of content from the thesis.

Conformément à la loi canadienne sur la protection de la vie privée, quelques formulaires secondaires ont été enlevés de cette thèse.

Bien que ces formulaires aient inclus dans la pagination, il n'y aura aucun contenu manquant.

Canada

Reproduced with permission of the copyright owner. Further reproduction prohibited without permission.

ABSTRACT

A novel MEMS ultrasonic sensor has been developed that exploits the Single Bubble Sonoluminescence (SBSL) phenomenon to realize a highly efficient energy transduction mechanism from the acoustical to electrical domain. In the developed system, highly stable laser like short duration light pulses are emitted when ultrasound waves strike a thermally generated microbubble stabilized in a small volume of de-gassed water confined within a MEMS fabricated micro-chamber. A photodetector detects these light pulses to generate an equivalent photo-current. The chamber geometry is 150 μm in diameter and 300 μm in height and is expected to have a sensitivity of 520 μA/atm.

Dielectrophoresis (DEP) along with capacitive sensing techniques have been used to stabilize the bubble at the center of the micro-chamber.

Since there are no vibrating diaphragms or deformable structures as commonly found in capacitive or piezoelectric ultrasound sensors, the sensor is free from any pull-in effects and stress related nonlinearities and limitations.

The sensor can be used in applications to detect high pressure ultrasound waves where conventional technology is not suitable.

Reproduced with permission of the copyright owner. Further reproduction prohibited without permission.

DEDICATION

To my friends and family

Reproduced with permission of the copyright owner. Further reproduction prohibited without permission.

ACKNOWLEDGEMENTS

There were many people who helped me through out the course of this project, and I would now like to take the chance to thank you all.

I would like to thank my Advisor, Dr. Sazzadur Chowdhury, without your guidance and support this project would never have come to fruition. Thank you for keeping my research on track and helping me remain focused.

Matthew Meloche, you've been one of my long time friends and colleagues. I wouldn't have been able to complete this without your support and your insight. Thank you. .

Ashkan Hosseinzadeh Namin, I'd like to thank you for putting up with my continuous plethora of questions. Your help was invaluable in making this thesis a work of art.

And finally, I would also like to thank NSERC and CMC for their generous funding, if it weren't for your generosity, this project could never have even begun.

Reproduced with permission of the copyright owner. Further reproduction prohibited without permission.

TABLE OF CONTENTS

Reproduced with permission of the copyright owner. Further reproduction prohibited without permission.

Reproduced with permission of the copyright owner. Further reproduction prohibited without permission.

Reproduced with permission of the copyright owner. Further reproduction prohibited without permission.

LIST OF TABLES

Reproduced with permission of the copyright owner. Further reproduction prohibited without permission.

LIST OF FIGURES

Reproduced with permission of the copyright owner. Further reproduction prohibited without permission.

Reproduced with permission of the copyright owner. Further reproduction prohibited without permission.

CHAPTER 1

INTRODUCTION

1.1 Thesis Objectives

The objective of this thesis is to design a MEMS based ultrasonic sensor that exploits a recently discovered phenomenon known as Single-Bubble sonoluminescence (SBSL) to realize a highly efficient energy transduction mechanism between the acoustical to electrical domain. In the developed system, highly stable laser like short duration light pulses are emitted when ultrasound waves strike a thermally generated microbubble stabilized in a small volume of de-gassed water confined within a MEMS fabricated micro-chamber. A photodetector detects these light pulses to generate an equivalent photo-current.

Reproduced with permission of the copyright owner. Further reproduction prohibited without permission.

Ultrasonic actuation and sensing is used widely in applications such as medical imaging, automotive collision avoidance systems, proximity detection, thermosonic chip bonding, etc. [1]. In recent years, there have been significant developments in high performance MEMS-based bulk or surface micromachined capacitive type ultrasonic sensors [1-2]. The capacitive type sensor transduction is popular due to it's good scaling properties, relatively higher sensitivity, possibility of realizing radically new design concepts, and low-power consumption [1-2]. A surface micromachined capacitive type ultrasonic sensor consists of a thin conducting diaphragm separated from a fixed ground plane by an air gap as shown in Figure 1. As the ultrasonic sound waves strike the diaphragm, the diaphragm deforms resulting in a change in capacitance between the diaphragm and the fixed back plate. A capacitive readout circuit is used to convert this capacitance change into a useful voltage signal.

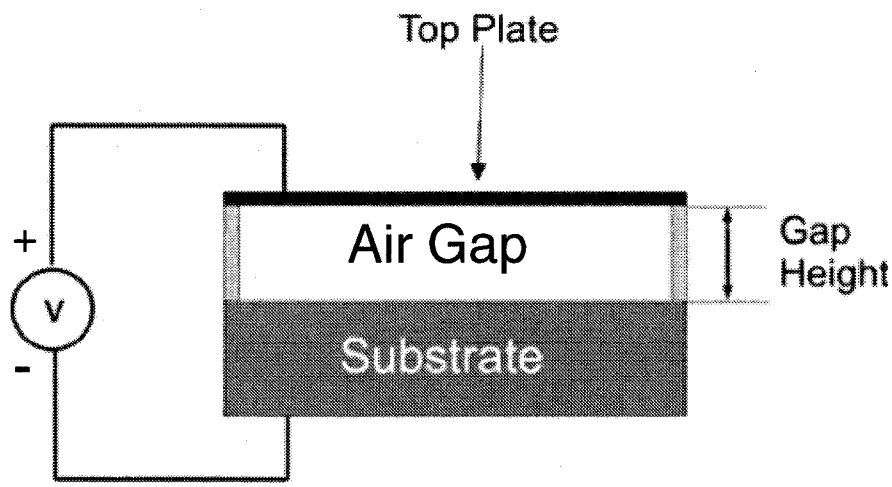

Figure 1. Conceptual cross-section of a capacitive type ultrasonic sensor.

Reproduced with permission of the copyright owner. Further reproduction prohibited without permission.

However, capacitive type sensors suffer from a dynamic range limited to little more than one-third of the air gap to avoid the diaphragm collapse due to the pull-in phenomenon [3]. The pull-in phenomenon occurs when the total applied electrostatic force due to the bias voltage overcomes the elastic restoring force of the diaphragm [3]. Additionally, the sensitivity of such capacitive type sensors depends on other factors such as, air streaming resistance and damping, stiffness, and nonlinear deformation of the diaphragm [3-5]. These issues limit the application of this type of ultrasonic sensor.

Alternative implementations of MEMS ultrasonic sensors rely on piezoresistive properties of materials to convert ultrasonic sound energy to electrical energy. A conceptual cross-section of this piezoresistive ultrasonic sensor is shown in Figure 2. When the piezoresistive thin film is bent or deformed due to an external force, an electric output can be obtained that is proportional to the strain measured in the piezoresistive material. The operating frequency of these ultrasonic sensors is dependant on the thickness of the piezoresitive film [3]. When the piezoresistive film is very thin, the membrane is susceptible to mechanical failure, if the external ultrasonic pressure field is large.

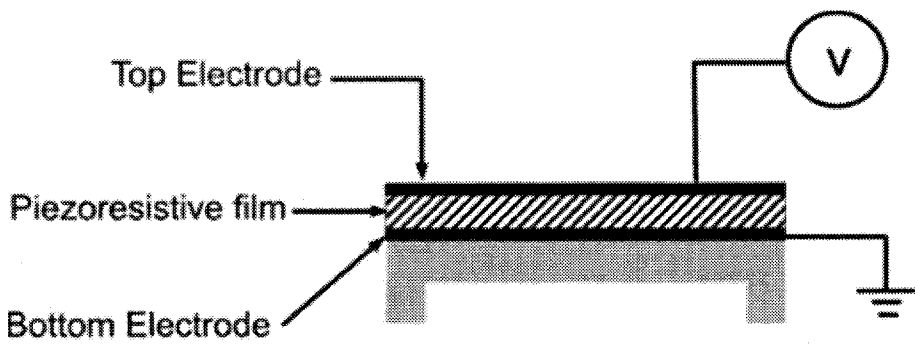

Figure 2. Conceptual cross-section of piezoresistive type ultrasonic sensor.

Reproduced with permission of the copyright owner. Further reproduction prohibited without permission.

Additionally, the sensitivity of piezoresistive ultrasonic sensors is relatively much lower compared to the capacitive ones.

A recently discovered physical phenomenon known as the Single Bubble Sonoluminescence (SBSL) [2, 7-9] offers the possibility of realizing a new type of MEMS based ultrasonic sensor that can overcome the limitations of capacitive type or piezoresistive type ultrasonic sensors. SBSL generates highly stable and precise short duration light pulses when a bubble suspended in a liquid collapses due to an applied ultrasonic pressure field [2, 7-9]. In the macro-scale, SBSL is achieved by stabilizing a bubble in the center of a spatially symmetric container using a resonant sound field. During the negative portion of the incident pressure wave, the bubble expands up to 10 times its normal radius, resulting in a large pressure difference on opposite sides of the bubble wall. The pressure difference causes the bubble to collapse catastrophically and releases approximately 10^6 photons per acoustical cycle [2, 7-9]. Compared to the mechanical work exerted on a single molecule by the driving resonators, this represents an energy amplification of 13 orders of magnitude [2, 7-9]. Contrary to conventional transducers, where no energy amplification occurs during the transduction process itself, a higher sensitivity ultrasonic sensor can be realized if these emitted light pulses can be detected with a suitable photodetector.

The major design challenges associated with the proposed sensing scheme are determined as: (1) Generation and release of a bubble within a MEMS fabricated micro-chamber, (2) bubble stabilization in the center of the micro-chamber, and (3) photo-detection.

Reproduced with permission of the copyright owner. Further reproduction prohibited without permission.

There have been recent developments in micro-scale bubble and droplet generation [10-12] and manipulation using the technique of dielectrophoresis (DEP) [13]. This technique can be exploited to stabilize a microbubble at the precise center of a MEMS fabricated cylindrical micro-chamber. This eliminates the need for a large spherical flask and piezoelectric resonators to create a standing wave pressure field as is necessary in macroscale sonoluminescence [2, 7-9]. Generated light pulses can be detected by integrating photodetectors at suitable locations in a MEMS fabricated micro-chamber of suitable geometry and dimensions.

Without a deformable diaphragm as found in capacitive and piezoresistive sensing, this sensor will be able to withstand very high acoustical pressure without fear of collapse, resulting in a much larger dynamic range compared to conventional MEMS-based ultrasonic sensors. Additionally it will be free of any pull-in effects.

Based on this conceptual approach, the design of a new ultrasonic sensor has been presented. In the proposed scheme, a thermally generated microbubble [14] is to be stabilized using dielectrophoresis (DEP) techniques in the center of a MEMS fabricated micro-chamber. Light pulses emitted by bubble collapse due to the incident ultrasonic wave, are detected by a suitably integrated photodetector which generates an equivalent electrical signal to complete the transduction process.

1.3 Design Challenges

The design for the microsensor consists of four main functional segments:

1. Microbubble generation
2. Microbubble stabilization
3. Photodetection

Reproduced with permission of the copyright owner. Further reproduction prohibited without permission.

4. Fabrication process table development

Each of these design segments is associated with certain design difficulties.

1.3.1 Microbubble Generation

There are two difficulties inherent with microbubble generation. The repeatable generation of microbubbles of a known size is one of the major difficulties with the microsensor. There are numerous ways to generate a microbubble with a size of 5 μm in radius presented in the literature [1-2]. Each method has advantages and drawbacks, and each was examined to determine the main method of bubble generation for this microsensor. The second issue is designing a module that will consume minimal amounts of power, since power consumption is always a concern when dealing with electronic devices.

1.3.2 Microbubble Stabilization

The major difficulty that exists within the microbubble stabilization module is the design of a module that can be easily fabricated using the current MEMS fabrication processes. There are various methods of bubble stabilization and manipulation; however only a few have the required properties to allow sonoluminescence to occur.

1.3.3 Photodetection

The photodetection module has one main difficulty. The major challenge is that most photodetectors have poor quantum efficiencies within the visible spectrum. Quantum efficiency is a measure of the ability of a photodetector to create electron-hole carrier pairs from an incident photon of a given wavelength. Many types of photodetectors have been investigated to determine the most suitable photodetector for

Reproduced with permission of the copyright owner. Further reproduction prohibited without permission.

the photon wavelength emitted by sonoluminescence while maintaining manufacturability.

1.3.4 Fabrication

Many MEMS fabrication techniques are an outgrowth from microelectronic fabrication techniques. As such, MEMS fabrication is primarily based on planar processes. Creation of certain shapes and geometries can be extremely difficult or even impossible with the current level of process maturity. Sonoluminescence requires a spatially symmetric (sphere or cylinder) chamber. Creating a spherical object using current MEMS fabrication processes would be extremely difficult and costly. However, by combining a variety of current MEMS deposition techniques to deposit many layers of materials it is possible to create deep cylindrical shapes.

1.4 Principle of Operation

The MEMS microsensor is a combination of 3 main modules, the microbubble generation module, the microbubble stabilization module and the photodetection module. The microbubble generation module is used to generate a bubble of size 5 μm in radius. Once the bubble is generated and is free to move in the chamber, the bubble stabilization module engages. The bubble stabilization module is comprised of a set of five position sensors and a bubble manipulation module. Located at the midpoint of the micro-cylinder wall, sets of capacitive sensors are used to determine the position of the bubble. The bubble stabilization module is used to apply a force on the bubble to control the vertical position and trap the bubble in the center of the microchamber. Once the bubble is trapped and struck by an incident ultrasonic acoustical wave, sonoluminescence will occur and light pulses will be emitted. The light pulses created by the sonoluminescing

Reproduced with permission of the copyright owner. Further reproduction prohibited without permission.

bubble will be picked up by the embedded photodetection unit placed along the bottom of the microchamber to complete the acoustical to electrical transduction.

A conceptual diagram showing the proposed sensor is shown in Figure 3.

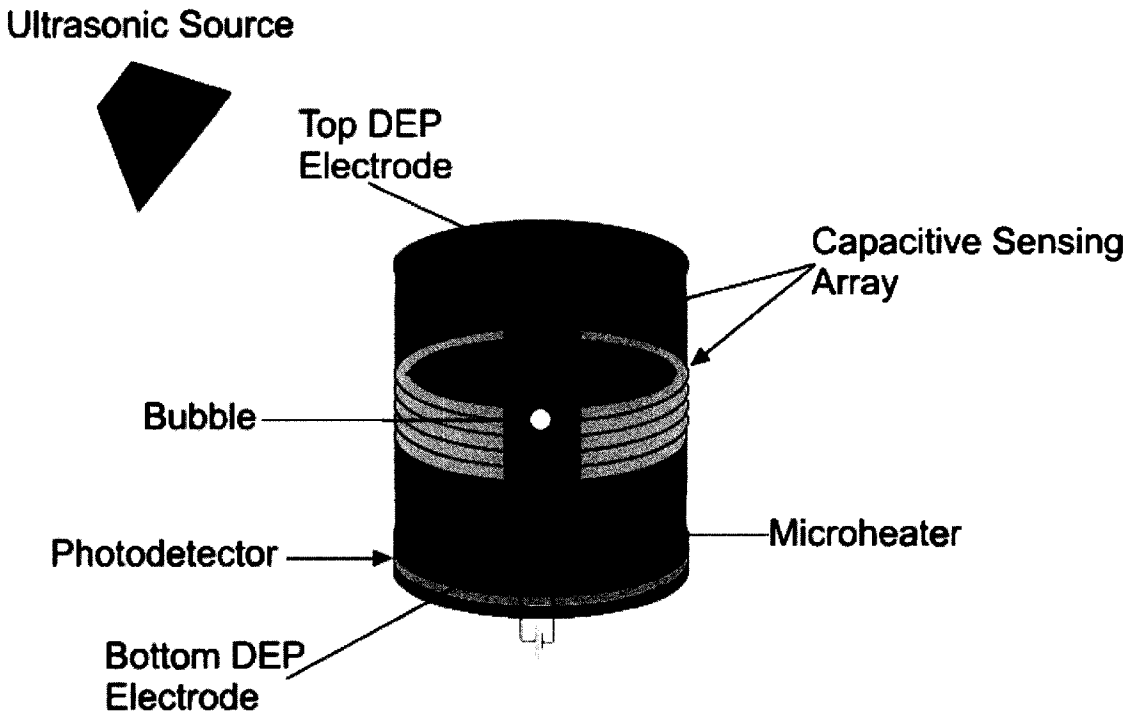

Figure 3. Conceptual diagram of the MEMS sonoluminescent ultrasonic sensor.

Reproduced with permission of the copyright owner. Further reproduction prohibited without permission.

1.5 Principle Results

The developed sensor has a diameter of 150 μm, a height of 300 μm, and exhibits a sensitivity of 520 μm/atm. Table 1 summarizes the major design specifications for the developed sensor.

Table 1: Microsensor Design Specifications

Parameter	Value	Unit
Sensor dimensions (Diameter x Height)	150 μm x 300	μm
Micro-heater (Length x Width x Height)	100 x 4 x 0.5	μm
Wall-to-wall electrode capacitance	14.87 (max), 6.15 (min)	pF
Operating frequency	25	kHz
Actuation voltage for bubble stabilization	200-400	V
DEP force	1.02	nN
Buoyancy force	1.02	nN
Sensitivity @ 80% quantum efficiency	520	μA/atm
Approx. number of charges on bubble surface	1.4×10^6	Coulombs
Power Consumption	1.183	mW

Reproduced with permission of the copyright owner. Further reproduction prohibited without permission.

1.6 Thesis Outline

Chapter 2 is an overview of the MEMS ultrasonic sensor. Sonoluminescence is described in detail.

Chapter 3 discusses the design of the microbubble generation module. General design considerations are treated here as well as mathematical modeling of this system and finite element analysis (FEA) simulation results to verify the behaviour of this module.

Chapter 4 details the design of the microbubble stabilization module. Exploration of the various design considerations and the mathematical modeling of this module will be elaborated; also the FEA simulation results are presented to verify the module behaviour.

Chapter 5 explores the various photodetection materials and identifies the most suitable photodetector topology. This chapter concludes with a detailed description of the selected topology.

Chapter 6 describes the fabrication process of the developed sensor. Using the available MEMS fabrication techniques an effective fabrication scheme will be described.

Chapter 7 provides a summary of work undertaken and the device concept, concluding with a discussion of device implementation and industry applications.

Reproduced with permission of the copyright owner. Further reproduction prohibited without permission.

CHAPTER 2

SONOLUMINESCENCE PHENOMENON

2.1 Sonoluminescence

Sonoluminescence is the emission of light by bubbles suspended in a liquid excited by sound, which provides a primary method of transduction for this microsensor. It translates energy from an acoustical wave into optical energy. The following sections describe the sonoluminescence phenomenon and how it can be exploited to realize a novel MEMS based ultrasonic microsensor.

2.2 Types of Sonoluminescence

There are two types of sonoluminescence:

1. Multi-bubble sonoluminescence (MBSL),

Reproduced with permission of the copyright owner. Further reproduction prohibited without permission.

2. Single-bubble sonoluminescence (SBSL).

Multi-bubble sonoluminescence was first discovered in 1934 by Fresnal and Schultes at the University of Cologne [2]. Fresnal and Schultes put an ultrasound transducer in a tank of photographic developer fluid. Their objective was to speed up the photographic development process. Instead, they noticed tiny dots on the film after developing, and realized that the bubbles in the fluid were emitting light with the ultrasound turned on. As a result the phenomenon known as multi-bubble sonoluminescence was discovered [2].

Single-bubble sonoluminescence (SBSL) was discovered in 1989 by Felipe Gaitan and Lawrence Crum [2]. Their method involved trapping a single bubble in an acoustic standing wave. The bubble would then emit light with each compression of the standing wave. This breakthrough allowed for a more systematic study of the phenomenon and isolated many of the complex effects into one stable and predictable bubble [2].

2.3 Macro Scale Theory of Sonoluminescence

In typical SBSL experiments, a spherical flask is used as the resonating chamber. Two piezoelectric type resonators are then glued onto into place diametrically opposed on the side of the flask. The flask is cleaned and then filled with de-gassed water. These resonators are used to create an acoustical standing wave within the spherical chamber. When the standing wave is stable, a highly accurate pipette is used to introduce a 5μm in radius microbubble into the flask. When the acoustical standing wave pressure field is strong enough to counteract the buoyancy force, the bubble will be stabilized at the precise center of the spherical flask as shown conceptually in Figure 4.

Reproduced with permission of the copyright owner. Further reproduction prohibited without permission.

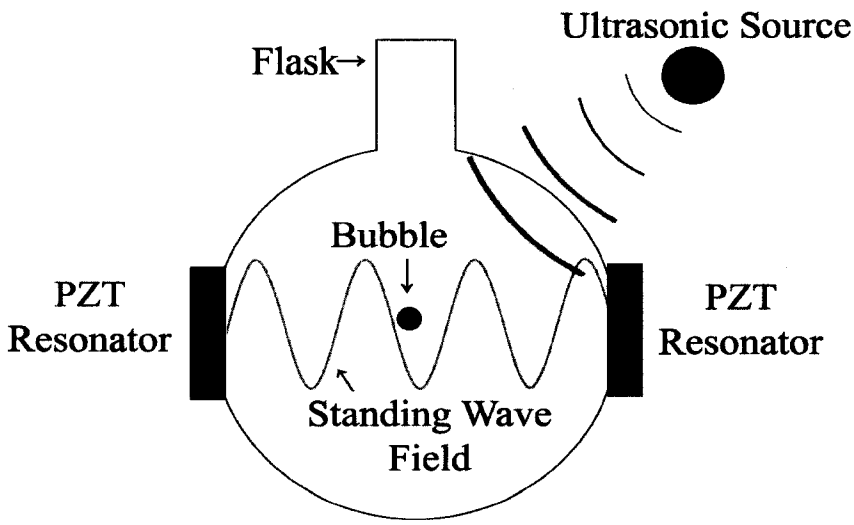

Figure 4. A bubble trapped inside the resonating chamber with an external ultrasonic source.

The diameter of the spherical flask is determined by the exciting frequencies of the piezoelectric resonators. The bubble is forced into the center of the resonating chamber by the ultrasonic sound field generated by the resonators due to the primary Bjerknes Force expressed as [8]:

$$F_{Bjerk} = V(t)\nabla p_e(r,z,t) \tag{1}$$

Where, $V(t)$ is the oscillating volume and $p_e(r,z,t)$ is the resonant sound field pressure. Since the introduced bubble has a fixed radius, the resonant sound field pressure can be expressed as [8]:

$$p_e(z,t) = p_{e,1}\cos(\omega_1 t)\cos(k_1 z) \tag{2}$$

Where, $\omega_1 = 2\pi f$ is the resonant frequency, $k_1 = 2\pi/\lambda$ is the wave number (this is the spatial analogue of frequency) and λ is the wavelength. When the primary Bjerknes force F_{Bjerk} is large enough to overcome the buoyancy force, F_g, associated with the

Reproduced with permission of the copyright owner. Further reproduction prohibited without permission.

bubble, the bubble will become trapped inside the resonating chamber [8]. The buoyancy force, F_g, associated with the bubble can be expressed as [8]:

$$F_g = (\rho_l - \rho_g)V(t) \times 9.81 \quad (3)$$

Where, $V(t)$ is the bubble volume, ρ_l and ρ_g are the liquid and gas densities, respectively. The trapped bubble is then subjected to a high amplitude ultrasonic wave and as the sound pressure field changes from rarefaction to compression, the bubble radius changes by up to 10 times its original size. As the volume increases, the internal pressure decreases causing a vacuum that collapses the bubble catastrophically. When the bubble catastrophically collapses it emits approximately 10^6 photons before reforming each acoustical cycle. Figure 5 shows the standing wave pressure field used to trap the microbubble. This pressure field will force the microbubble into the center of the spherical flask. Figure 6 shows the buoyancy forces of the bubble as the bubble radius expands and contracts. As the bubble radius expands the buoyancy forces increase. Figure 7 depicts the Bjerknes forces that counteract the buoyancy force. This traps the bubble vertically so it can not escape. A composite model for the bubble stabilization forces is shown in Figure 8. This shows that during a minima of the standing wave pressure filed, the buoyancy forces are at a maximum and the Bjerknes forces are equal to 1.02 nN. These combined effects trap the microbubble in the center of the chamber.

Reproduced with permission of the copyright owner. Further reproduction prohibited without permission.

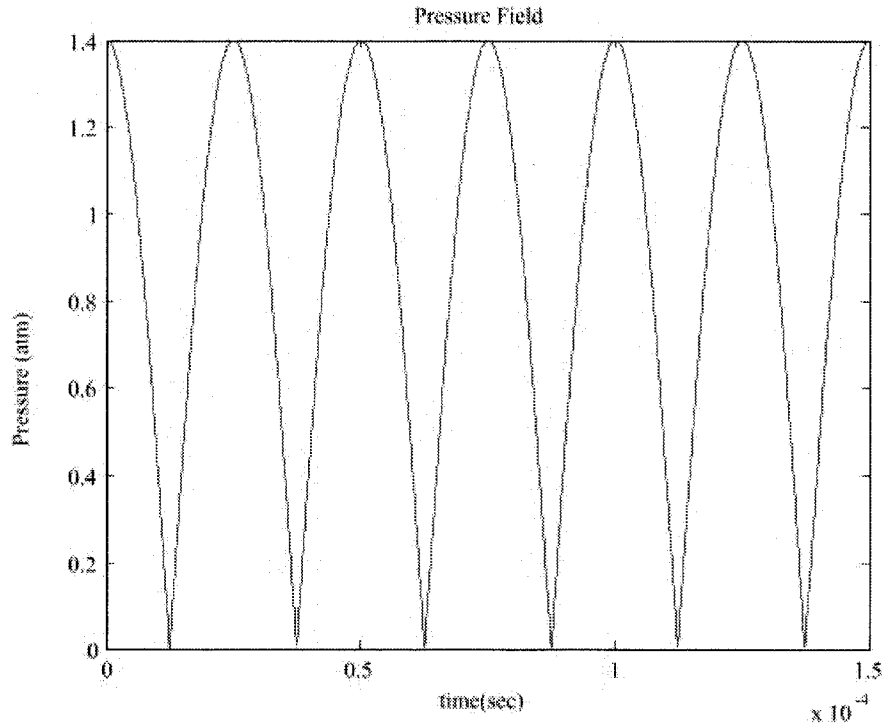

Figure 5. Standing wave pressure field.

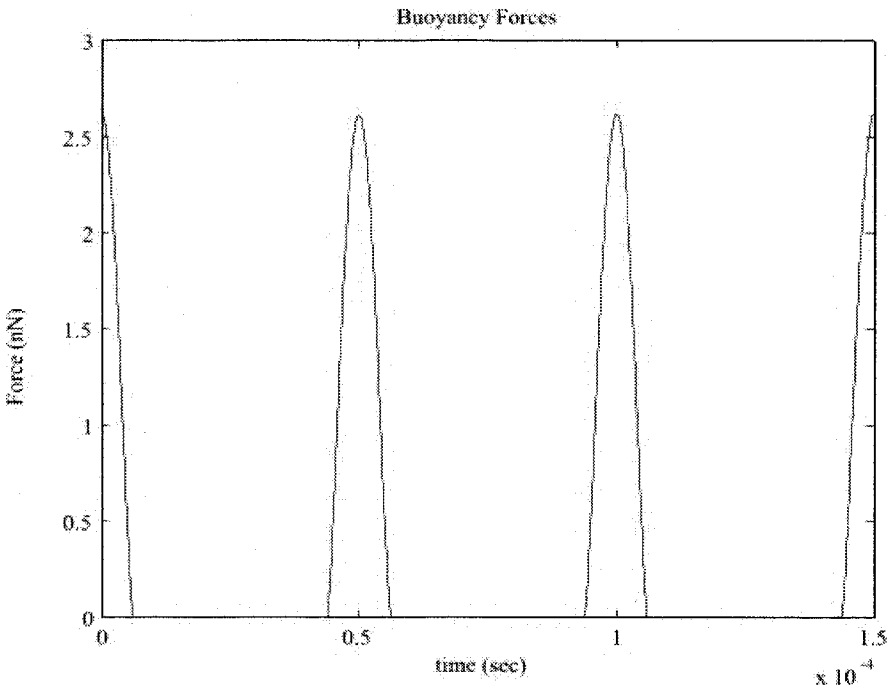

Figure 6. Buoyancy force of the microbubble.

Reproduced with permission of the copyright owner. Further reproduction prohibited without permission.

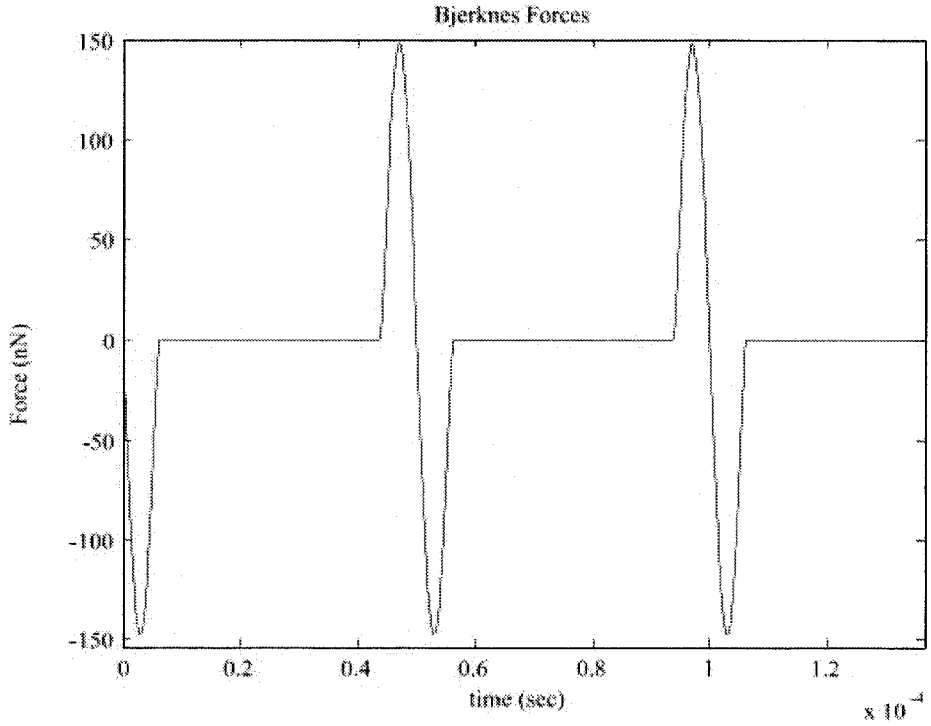

Figure 7. Bjerknes forces used to trap the microbubble.

2.3.1 Bubble Dynamics

Ultrasonic forces in the liquid are caused by the piezoelectric transducers glued to the sides of the spherical flask. These transducers are tuned to the lowest resonant frequency of the container. The frequency is approximately 25 kHz and the amplitude of the driving pressure at the center of the container is 1.2 atm for SBSL to occur [2, 7-9]. The dynamics of the motion of the bubble is characterized to a first approximation by the Rayleigh-Plesset equation [2]:

$$R\ddot{R} + \frac{3}{2}\dot{R}^2 = \frac{1}{\rho}\left(p_g - P_0 - P(t) - 4\eta\frac{\dot{R}}{R} - \frac{2\gamma}{R} \right) \tag{4}$$

Equation (4) is an approximate equation that is derived from the Navier-Stokes

Reproduced with permission of the copyright owner. Further reproduction prohibited without permission.

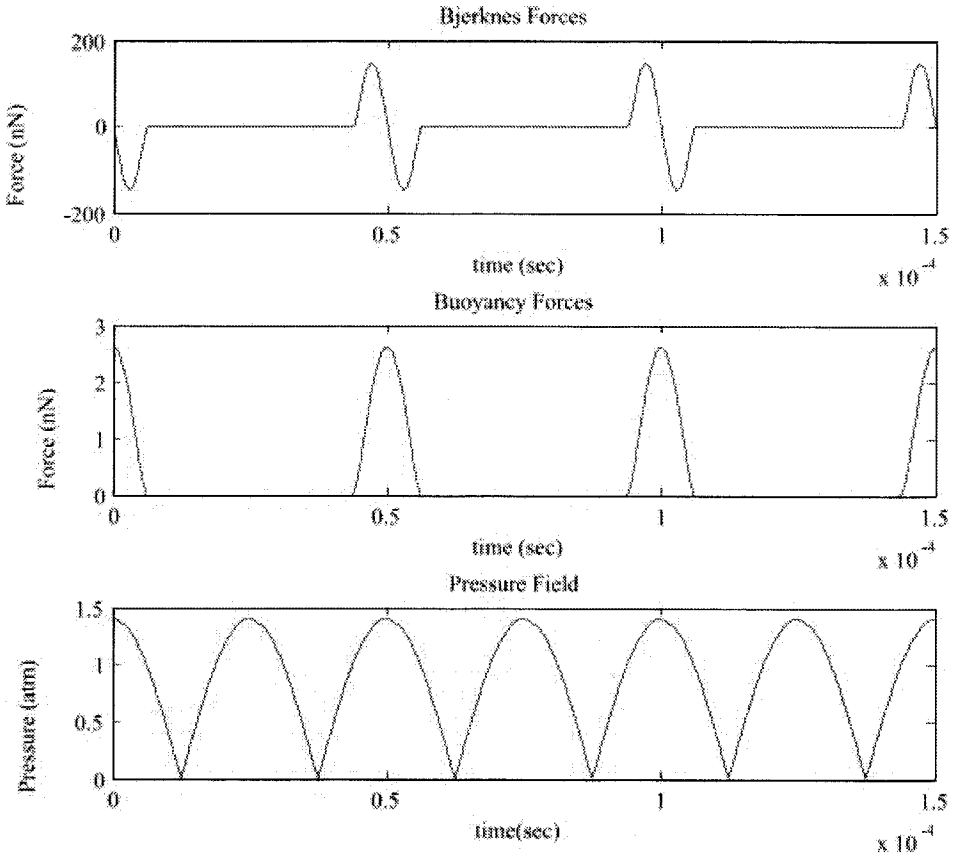

Figure 8. Composite image of Bjerknes, buoyancy and the pressure field. The bubble is trapped once the buoyancy and the Bjerknes forces are equal.

equations for compressible fluids [2, 7-9]. It describes the change in radius of the bubble, R, as a function of time t, where η is the viscosity, ρ the pressure, and γ is the surface tension [2, 7-9]. As the Rayleigh-Plesset equation is only an estimate, there are still some principle sources of error around surrounding the period of bubble collapse. These discrepancies are the main sources of modeling error for the theories of SBSL [2, 7-9].

Figure 9 shows a curve fitted plot of the bubble radius and acoustical pressure amplitude versus time for one cycle [2, 7-9].

Reproduced with permission of the copyright owner. Further reproduction prohibited without permission.

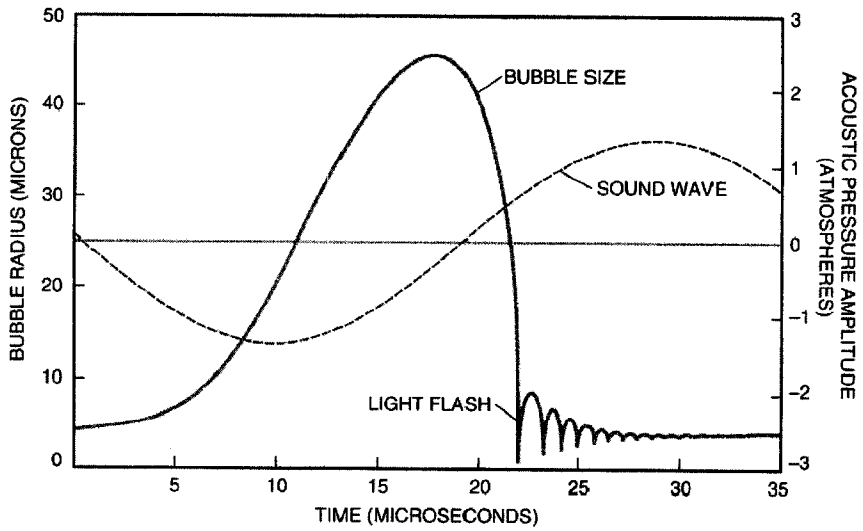

Figure 9. Measured bubble radius plotted for one acoustic cycle. Courtesy of S. Putterman [7].

During the expansion period, which is also the negative portion of the driving pressure field, the applied tension causes the bubble to expand. This expansion continues until the driving pressure changes and becomes positive. The expansion allows the bubble to reach a maximum size up to 10 times the original size. During collapse, when the driving pressure becomes positive, the compressive forces of the drive pressure along with the low pressures inside the bubble cause the bubble to collapse. The bubble collapses and hits the Van Der Waal hard core radius at which point the bubble releases light [2, 7-9]. These light flashes last no longer than 100 ps and release approximately 10^6 photons of light per flash. The flash of light that emitted is in the visible range, a blue light having a wavelength of 450 to 550 nm [2, 7-9].

During the regeneration phase, also called the after bounces period, the bubble radius bounces around the Van Der Waal hard core radius before returning to the original size [2, 7-9].

Reproduced with permission of the copyright owner. Further reproduction prohibited without permission.

This completes one cycle of the sonoluminescence phenomenon. Once the bubble has regenerated, it is ready for the cycle to be repeated. There is one bubble collapse for every cycle of the ultrasonic drive pressure.

2.4 Conclusions

After reviewing the phenomenon as a transduction method from the ultrasonic domain to the optical domain it has been shown that this provides one of a small number of direct transduction mechanisms between the acoustic and optical domains. To realize a MEMS based microsensor based on SBSL, it is necessary to develop a method to generate the required diameter microbubbles, a method to trap the bubble inside a micro-chamber and a method for sensing the emitted pulses of light. From Figure 8, it can be observed that a Bjerknes force of 1.02 nN is required to counteract the buoyancy force of the microbubble. The driving amplitude of the external ultrasonic wave is 1.2 atm and the emission of 10^6 photons per flash of light is received every cycle. The pulse of light is mainly blue light. The wavelength of blue light is approximately 450 nm to 550 nm in length. This visible light can be transduced into a usable electrical signal by a suitable photodetector.

Reproduced with permission of the copyright owner. Further reproduction prohibited without permission.

CHAPTER 3

MICROBUBBLE GENERATION

3.1 Motivation

This chapter discusses in detail the design of a MEMS fabricated polysilicon microheater that is to be used for consistent radius microbubble generation. State-of-the-art methods in microbubble generation have been investigated and it has been determined that a MEMS polysilicon microheater is the most suitable for the proposed system.

3.2 Microbubble Generation

There are many different ways to generate (introduce) a bubble in water. The methods investigated are micropipettes which are similar to ink jet printer heads, and microheaters.

Reproduced with permission of the copyright owner. Further reproduction prohibited without permission.

3.2.1 Micropipette

Micropipettes are used to inject precise amount of fluids in applications such as ink jet or bubble jet printers. In ink jet printer heads, thermally grown bubbles are used to squeeze out a microdroplet of ink [10]. These droplets are very accurate in size and can be controlled to dispense an exact amount of fluid. The second type of micropipette based droplet injection mechanism is similar to a hypodermic needle [10]. This mechanism uses a mechanical plunger to force out a controlled amount of liquid as shown in Figure 10 conceptually [10]. For this mechanism, the volume displaced within the container is equal to the volume that is ejected from the nozzle.

3.2.2 Microheater

Microheaters create bubbles similar to kettle boiling water on a stove. The surface heats up past the boiling temperature of water and will nucleate a bubble onto the heated

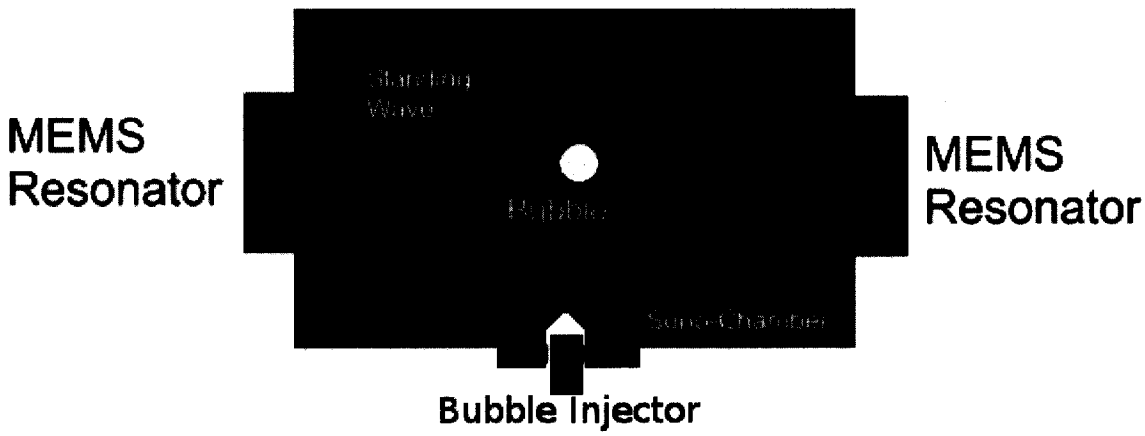

Figure 10. Conceptual diagram of a micropipette bubble injector.

Reproduced with permission of the copyright owner. Further reproduction prohibited without permission.

surface. When the bubble reaches a certain size, the buoyancy forces overcome the surface tension which allows the bubble to lift off the surface and float away. Microheaters are constructed of specific materials which tend to be hydrophilic to facilitate bubble release. Currently, materials such as gold or polysilicon are used [10]. Polysilicon can be fabricated, using careful doping methods, into a micro sized resistor. This resistor can then be heated quickly to generate microbubbles. To ensure the expeditious release of the bubble the microheater can be electrostatically actuated momentarily to facilitate the release of the stuck bubble as shown in Figure 11.

3.2.3 Bubble Nucleation

When a liquid is heated in the presence of a solid surface, heterogeneous bubble nucleation occurs. This produces many bubbles across the entire surface [10–11].

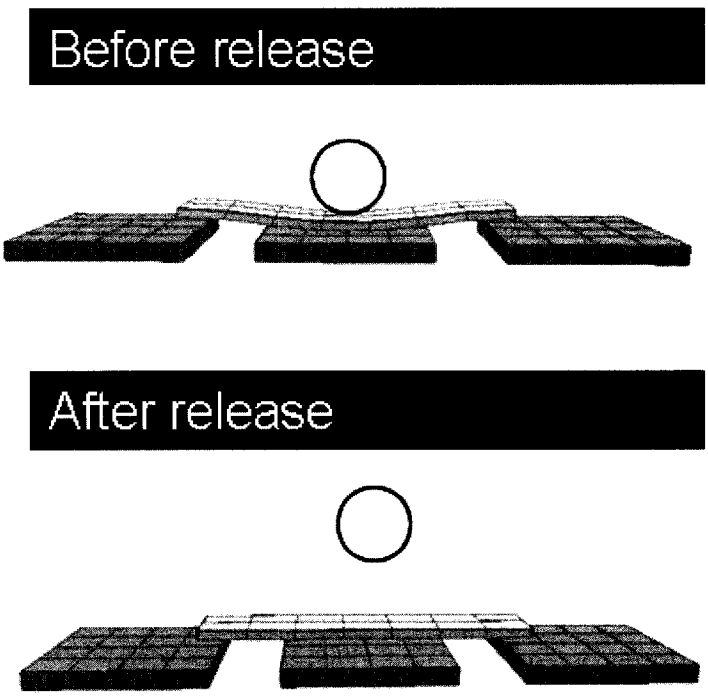

Figure 11. Microheater microbubble generation module releasing a stuck microbubble.

Reproduced with permission of the copyright owner. Further reproduction prohibited without permission.

However, it has been observed in this regime that the initial bubbles formation takes place in surface defects and cavities, known as surface cleats. The temperature required to nucleate a bubble in a surface cavity is inversely dependant on the cavity radius, as shown in the following equation [10–11]:

$$T_w - T_{sat} = \frac{2\sigma T_{sat}}{h_{lv}\rho_v r_c} \tag{5}$$

where T_w is the surface temperature, T_{sat} is the saturation temperature of water (373°K), σ is the surface tension (5.89×10^2 N/m), h_{lv} is the latent heat of vaporization (2.26×10^2 J/kg), ρ_v is the vapor density (0.60 kg/m^3 for water), and r_c is the radius of the cavity. For cavities of 1 μm in radius, a temperature of at least 136°C would be required to heterogeneously nucleate single bubbles [10-11], whereas for cavities of 0.2 μm in radius, the required thermodynamic superheat needed to nucleate a bubble is 256°C [10-11]. Surface cavities with radii smaller than this would spontaneously nucleate before they were formed in the surface cavity [10-11]. With a bubble cavity of 1 μm, it is possible to control heterogeneous nucleation in this surface cavity.

3.2.4 Resistive Heating

Resistive heating provides a well understood, easily localized transduction mechanism between the electrical and thermal domains. Energy transferred to vaporize the water can be calculated through resistive dissipation and the thermodynamic heat flow of the system. A table summarizing the characteristics of water is shows in Table 2.

Reproduced with permission of the copyright owner. Further reproduction prohibited without permission.

Table 2: Properties of Water

Parameter	Value	Unit
Liquid Density	1000	kg/m^3
Surface Tension	$5.89x10^2$	N/m
Latent Heat of Vaporization	$2.26x10^2$	J/kg
Vapor Density	0.60	kg/m^3

From a known bubble volume and a given density, the bubble mass is calculated with the following equations:

$$M = \frac{D}{V} \tag{6}$$

$$V = \frac{4}{3}\pi r^3 \tag{7}$$

Where, M is the mass, D is the density, V is the volume, and r is the bubble radius. For a bubble with the radius of 5 μm, a mass of 523.6 picograms is calculated using the density of water. The amount of energy required to vaporize the mass of the bubble can be found using:

$$E = h_{lv}M \tag{8}$$

Where, E is the energy, h_{lv} is the latent head of vaporization of water and M is the mass [10–11]. The energy required to generate a microbubble of this size is calculated to be 0.1183 mJ. The control of the bubble size is highly dependant on time. The longer the current is applied, the larger the generated bubble. For a vaporization time of 1.0 millisecond, the required power can be calculated to be equal to be 1.183 mW.

Reproduced with permission of the copyright owner. Further reproduction prohibited without permission.

The resistance for a thin film of polysilicon can be determined from:

$$R = \frac{L}{TW\sigma_e} \tag{9}$$

Where, R is the resistance, L is the length of the microheater, T is the thickness, W is the width and σ_e is the electrical conductivity [14]. Finally, using the following equation:

$$P = I^2 R \tag{10}$$

The required current can be determined knowing the resistance and the power to be equal to 0.4 mA. In Table 3, the physical properties of polysilicon have been summarized that were used to design the fixed-fixed beam microheater.

3.3 Design Solution

Both resistive and injection based methods of bubble generation were investigated. Based on the current MEMS technology the complexity of integrating a MEMS based micropipette is extremely high. It has been determined that the best solution for this would be to design a simple fixed-fixed beam microheater. This type of heater would allow for a bubble to be generated on the surface of the heating strip.

Table 3: Polysilicon Properties

Parameter	Value	Unit
Electrical Resistance (R)	8300	Ω•cm
Thermal Conductivity (κ)	148	W/K-m
Density (ρ)	2330	kg/m^3
Specific Heat (C_m)	712	J/Kg-K
TCR (α_r)	$2500x10^{-6}$	K^{-1}

Reproduced with permission of the copyright owner. Further reproduction prohibited without permission.

If the microbubble was not released after creation, the fixed-fixed beam style microheater can be momentarily vibrated to release the microbubble as shown in Figure 11. Detailed specifications of the designed microheater based on the concepts discussed in previous sections are listed in Table 4.

The designed microheater has been simulated using IntelliSuite™ and the generated 3-D geometry of the microheater inside the microchamber is shown in Figure 12.

3.4 Conclusions

A 5 μm microbubble can be generated consistently using small amounts of current. The fixed-fixed beam microheater provides a controllable, repeatable bubble generation mechanism which is more easily manufactured then an injection based solution. The microheater can be implemented using a relatively small number of fabrication steps based on standard MEMS fabrication processes. During operation the module draws 0.4 mA to generate a microbubble and consumes 1.183 mW of power. The Maximum temperature that the design of this microheater can attain is 150°C. The microheater requires 136°C to nucleate a bubble with a surface cleat of 1 μm.

Table 4: Microheater Design Specifications

Parameter	Value	Unit
Dimensions	100 x 4 x 0.5	μm
Temperature	150 Max.	°C
Cavity Radius	1	μm
Current	0.4	mA
Power	1.183	mW

Reproduced with permission of the copyright owner. Further reproduction prohibited without permission.

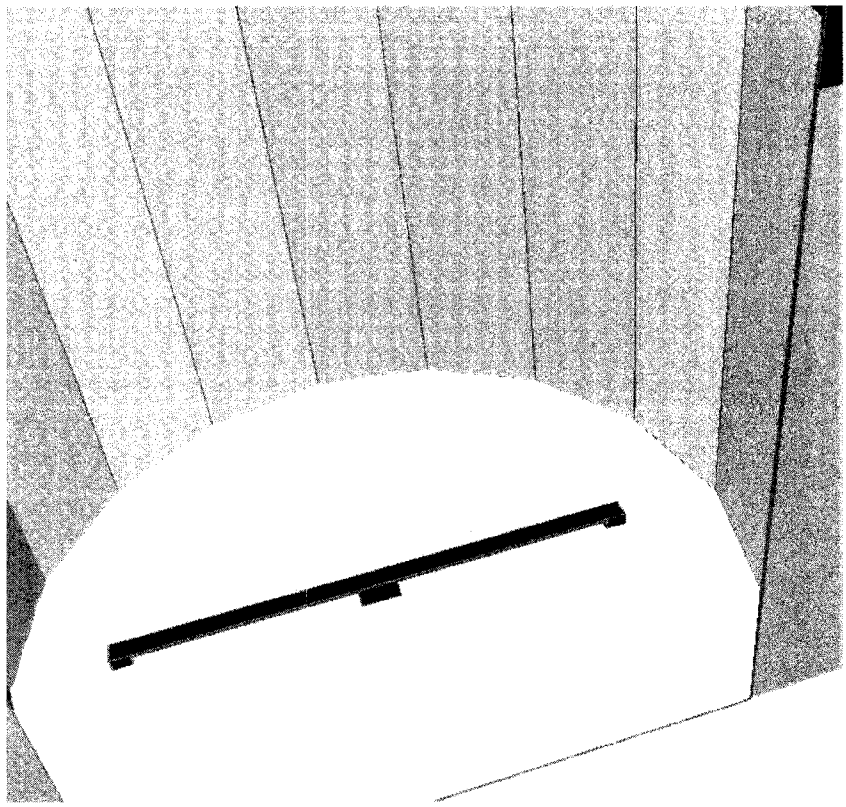

Figure 12. Microheater simulated in IntelliSuite™.

The microheater also inherently has a bubble release mechanism in the event that the bubble is stuck to the surface of the microheater. Using this type of module limits the amount of mechanical elements in the modules. Limiting the amount of mechanical elements decreases the chance of mechanical failure while increasing the maximum operating pressure the sensor can withstand.

Reproduced with permission of the copyright owner. Further reproduction prohibited without permission.

CHAPTER 4

MICROBUBBLE STABILIZATION

4.1 Motivation

For single-bubble sonoluminescence (SBBL) to occur, a microbubble must be stabilized in the center of the cylindrically shaped microchamber. In the macroscale, the bubble stabilization is carried out using standing waves generated by piezoelectric ultrasonic transmitters attached to the spherical resonating flask. For the proposed cylindrically shaped MEMS sensor, investigation has been made to determine a suitable solution for this bubble stabilization problem. In this chapter, a summary of different possible solutions has been discussed and a dielectrophoresis based bubble manipulation technique along with a capacitive sensing mechanism has been determined to be the best for the proposed microsensor. Detailed specifications for the dielectrophoresis based

Reproduced with permission of the copyright owner. Further reproduction prohibited without permission.

bubble manipulation technique along with a capacitive sensing mechanism have been determined while considering the fabrication issues.

4.2 Microbubble Stabilization

In order for sonoluminescence to occur, a microbubble must be stabilized into the center of a spherical or cylindrical chamber. The microsensor in this thesis will use a cylindrically shaped chamber. Once the bubble is stabilized the chamber can be bombarded with an ultrasonic exciting signal to allow sonoluminescence to occur. The object of this chapter is to determine the best design for a module that will allow for microbubble manipulation and microbubble position sensing.

4.2.1 Piezoelectric Resonators

In the macroscale experiments piezoelectric resonators are used to provide the stabilization forces required to position the bubble within the chamber. Piezoresonators as seen in Figure 13 are could be fabricated and would provide adequate bubble stability in the microscale. However, since a standing wave is required within the length of the chamber, using a piezoelectric resonator is not a possible solution for the proposed sensor geometry. The length of a 25 kHz standing wave is 13.3 mm, which is much longer than the length of a cylindrical MEMS microchamber. Since the length of the standing waves that are required in the macroscale experiments are too long for the microchamber. Piezoelectric microresonators are not suitable for this application.

Reproduced with permission of the copyright owner. Further reproduction prohibited without permission.

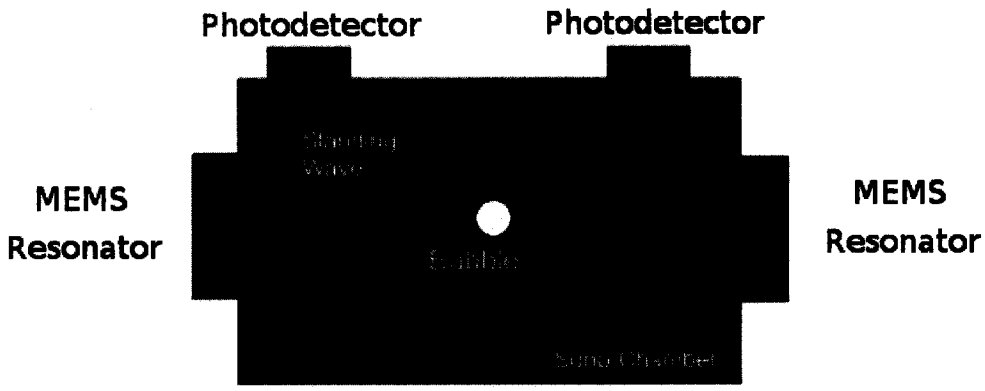

Figure 13. Conceptual diagram of a microresonator used to stabilize a bubble.

4.2.2 MEMS Micropincers

Another design solution was a mechanical stabilizer. This design involves the use of a pair of micropincers or a v-groove combined with surface tension to mechanically "hold" the microbubble. A conceptual diagram of the v-groove style bubble stabilization module is shown in Figure 14. The v-groove device has a heating wire that allows the bubble to be formed. Due to the surface tension between both sides of the v-groove fingers the bubble would get held by these fingers and be stabilized at the center of the chamber. However, the main problem with this type of stabilization mechanism is that the surface tension that is used to hold the bubble in place will not allow sonoluminescence to occur. So this type of stabilization technique can not be used.

Reproduced with permission of the copyright owner. Further reproduction prohibited without permission.

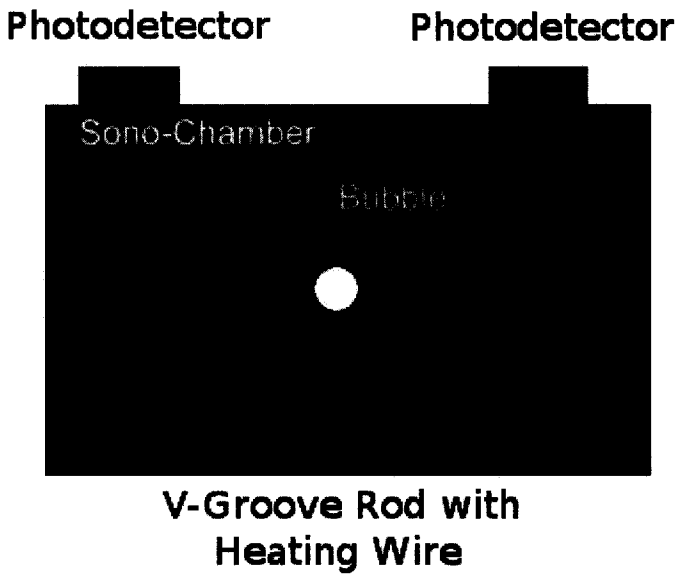

Figure 14. V-groove micropincer stabilization mechanism.

4.2.3 Electrokineteics

Another method for stabilizing a bubble that was investigated is the ability to use electrokinetics. Electrokinetics is the study of the motion of particles that result from an electric potential difference. This motion is generated by an electromagnetic force that is created between electric potentials. This force causes the particle to move in a given direction. By controlling the amount of potential difference it is possible to determine the amount of force generated. This is extremely convenient for the proposed microsensor as electrokinetics at the microscale works very well since the force generated by the potential difference increases exponentially as the gap between the potentials is reduced. The solution contains no movable structures allowing it to withstand high amplitude signals while allowing for the microbubble to be manipulated with a good degree of accuracy. It makes for a suitable solution for the scope of this thesis.

Reproduced with permission of the copyright owner. Further reproduction prohibited without permission.

4.3 Dielectrophoresis

The technique of dielectrophoresis and/or electrorotation (commonly known as electrokinetics) is used in biology to manipulate and separate particles at the cellular level [12-13]. However, in recent years, use of the technique has been expanded into the field of nano and microtechnology, due to the precise ability to manipulate particles in these ranges [13, 15].

Following the theory of dielectrophoresis (DEP), when a particle is subject to an external electric field, the electric field creates a dipole within the particle. If the external electric field is non-uniform, as in a field gradient, the field will exert a net force on the particle and there will be movement as seen in Figure 15. This force will either move the particle towards the high or low density field region, depending on the relative permittivity (a physical quantity that describes how an electric field is affected by a dielectric medium) of the particle compared to the surrounding medium [13, 15]. If the permittivity of the particle is greater than that of the surrounding medium, the force will be towards the higher density field region. This is referred to as positive DEP. Otherwise the force exerted on the dipole will be opposite, and the particle moves towards the region of lowest field density [13, 15]. Since the direction of the field is insignificant, the force can also be created by using an AC field [13]. The dielectrophoretic force that acts on a spherical particle is described as:

$$F_{DEP} = 2\pi R^2 \varepsilon_m \Re e\{K(\omega)\}\nabla E^2 \qquad (11)$$

Where, ε_m is the permittivity of the surrounding medium (for the purpose of this thesis the medium is water) E is the RMS electric field intensity, R is the radius of the bubble

Reproduced with permission of the copyright owner. Further reproduction prohibited without permission.

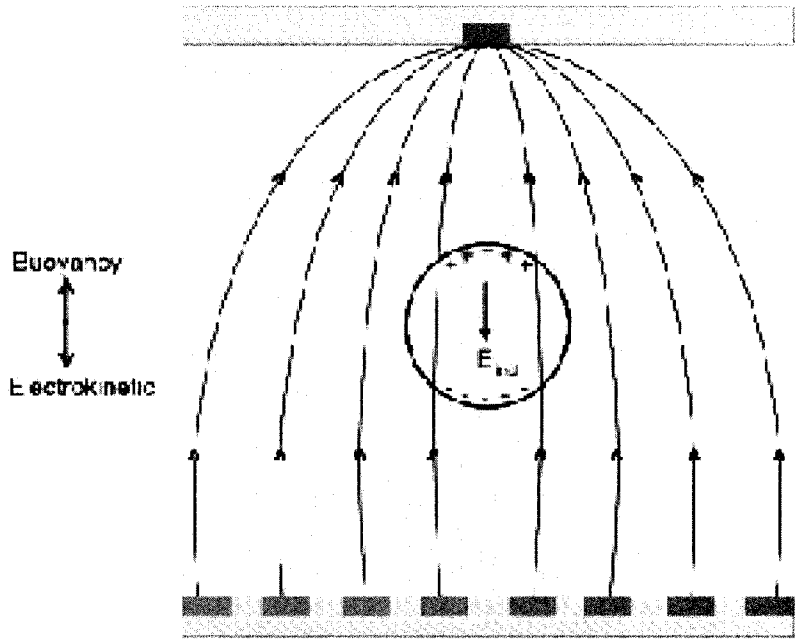

Figure 15. A particle under the influence of dielectrophoresis.

and $\Re e\{K(\omega)\}$ is the real part of the Clausius-Mossotti factor, expressed as [13]:

$$K(\omega)=\frac{\varepsilon_p^*-\varepsilon_m^*}{\varepsilon_p^*+2\varepsilon_m^*} \tag{12}$$

Where, ε_p^* and ε_m^*, and represent the complex permitivities of the medium and the particle respectively [13, 15]. Using the Gauss's law, described as:

$$V(x)=\int\frac{\rho(x)}{\varepsilon}\delta x \tag{13}$$

and

$$\nabla E=\frac{\rho}{\varepsilon} \tag{14}$$

The dielectrophoretic force can be determined easily for a particular voltage. The quantity ρ in (14) represents the electric charge density.

Reproduced with permission of the copyright owner. Further reproduction prohibited without permission.

The charging of micro-droplets can be done through several methods. One of these methods is electrical double layer charging [10]. This method is used to control the velocity and position of suspended liquid droplets between parallel plates using a large electric field. In order for this actuation method to work, the bubble must be charged. The Rayleigh limit [10] of microdroplet charging describes the maximum amount of charge that can be stored on a microdroplet, before the internal repulsive forces from like charges stored on the surface exceed the surface tension. This limit is the same for a micro-bubble inside a liquid. The Rayleigh limit, can be derived from [10]:

$$N = \frac{1}{e}(2\pi\gamma)^{\frac{1}{2}}(d)^{\frac{3}{2}} \tag{15}$$

Where, N is the number of electron charges, γ is the fluid surface tension and d is the bubble diameter. For water, γ = 72.7 dyne/cm that yields approximately 1.4 x 10^6 charges for a bubble radius of 5.0 μm. Based on this quantity of charge, the necessary actuation voltage for dielectrophoresis can be determined. The amount of force required to counteract the buoyancy force of the microbubble is 1.02 nN.

Two main DEP electrodes are placed within the chamber, by using highly doped polysilicon as the main DEP electrode along the upper edge of the chamber, and a smaller electrode beneath the polysilicon microheater. Finite element analysis (FEA) was carried out using the IntelliSuite™ MEMS design tools and it was determined that at an actuation voltage of 255 V is necessary to generate the required force of 1.02 nN using the DEP electrodes. At an actuation voltage of 400 V the DEP electrodes, as seen in figure 16, can produce a maximum actuation force of 1.66 nN. This provides more than enough force to counteract the buoyancy force and will force the bubble back into center of the cylinder if it floats beyond the mid point of the chamber.

Reproduced with permission of the copyright owner. Further reproduction prohibited without permission.

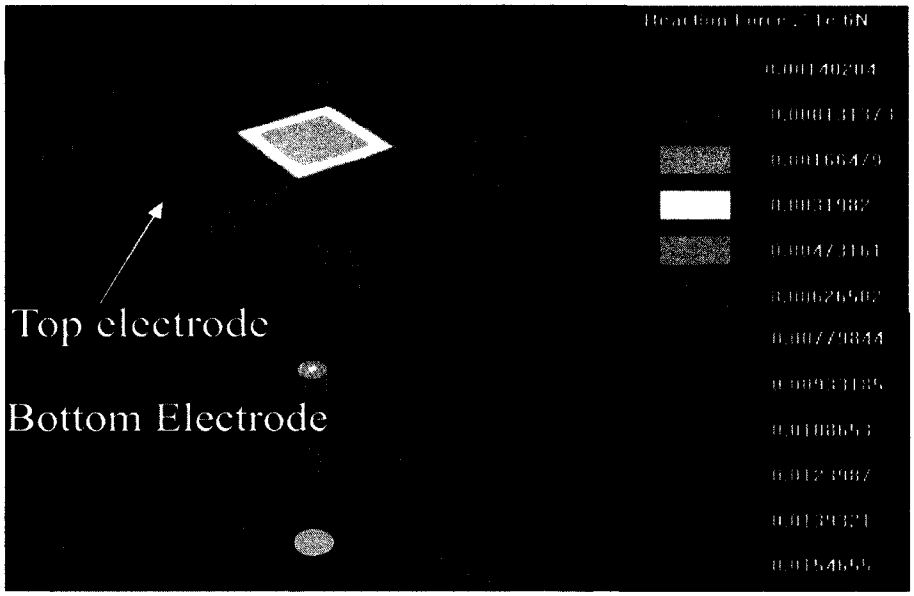

Figure 16. Dielectrophoresis FEA Simulation using IntelliSuite™.

4.4 Microbubble Position Sensing

By using dielectrophoresis to manipulate the bubble it is possible to actuate the elevation of the bubble within the chamber. To sense the elevation of the bubble as it ascends within the chamber requires a mechanism that can detect the presence of the bubble as it passes past the detector.

4.4.1 Capacitive Sensing

A capacitive sensing method has been developed to determine the position of the bubble as it ascends after release from the heater. By controlling the DEP forces along with the developed capacitive sensing technique, it is possible to stabilize the bubble in the precise vertical and radial center of the microchamber.

Reproduced with permission of the copyright owner. Further reproduction prohibited without permission.

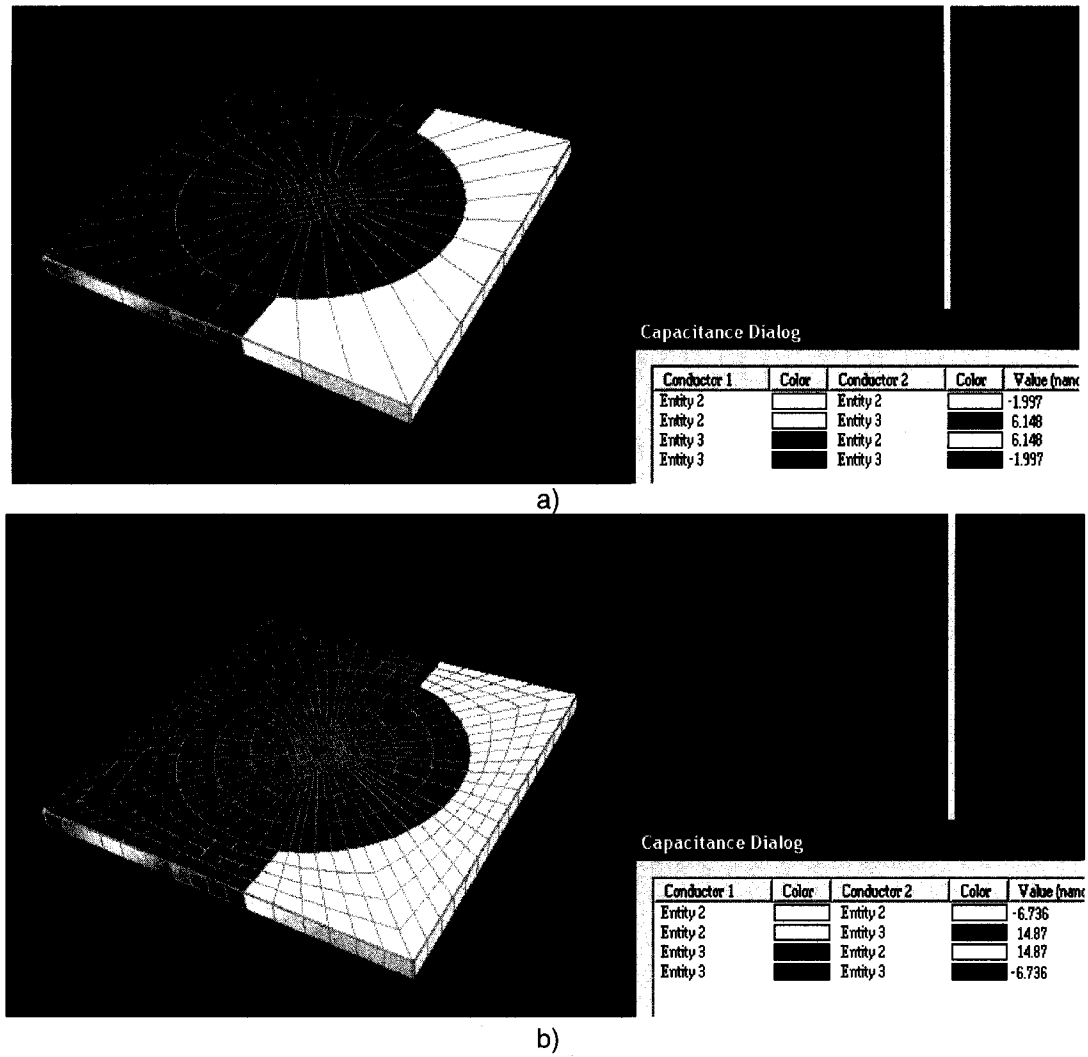

Figure 17. a) A single pair of capacitive sensing plates with no microbubble shows a capacitance of 6.15 pF. b) A single pair of capacitive sensing plates with a microbubble shows a capacitance of 14.87 pF.

Since the permittivity of the bubble and the water has a large variance, a capacitance change can be observed as the bubble passes between a pair of capacitive plate sensors. The capacitive sensing array will be fabricated using LPCVD polysilicon between layers of silicon dioxide. The silicon dioxide is used as an insulating layer to electrically isolate each capacitive sensing electrode. The capacitive sensors have been shown to have a minimum capacitance of 6.15 pF when no microbubble is present and a maximum capacitance of 14.87 pF when a bubble is present as shown in Figure 17. These

Reproduced with permission of the copyright owner. Further reproduction prohibited without permission.

capacitance simulations were done using the IntelliSuite™ FEA software package [16]. These capacitive sensing electrodes will be used to determine the vertical position of the bubble. A set of five capacitive sensing plates will be layered one atop another. This array of capacitive sensing plates will be placed along the walls of the microchamber to be used as the vertical position sensors for the bubble. During DEP, these capacitive plates can also be charged using the same polarity as the top DEP electrode. The electromagnetic field will also help push the bubble into the radial center of the chamber. A conceptual diagram of the capacitive sensing array and the electric fields generated to stabilize the bubble in the horizontal center of the chamber is shown in figure 18.

4.5 Conclusions

The bubble stabilization module incorporates another complex phenomenon known as dielectrophoresis as the vertical bubble positioning mechanism. This mechanism induces a dipole in a particle; for the scope of this thesis the particle is a

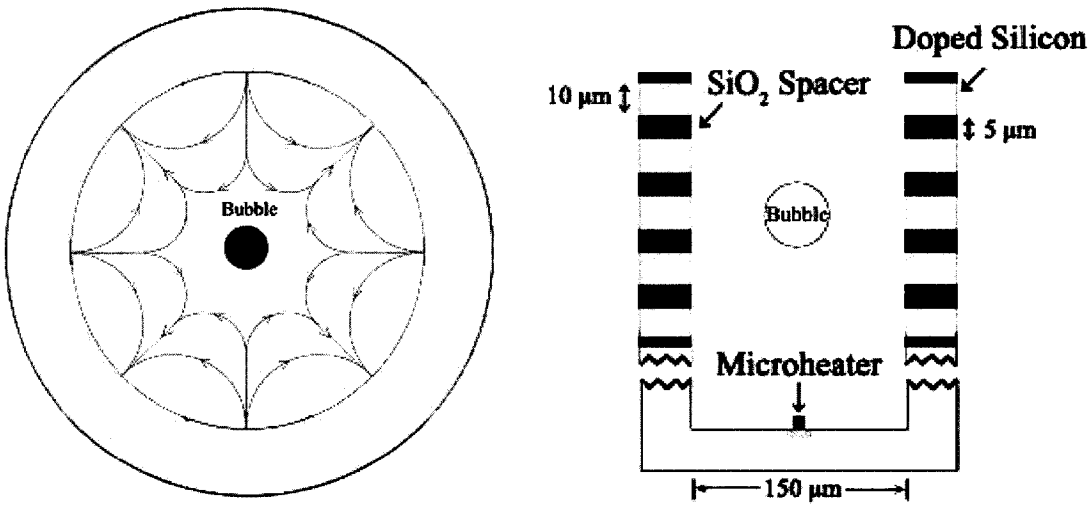

Figure 18. a) Conceptual diagram of the electric fields used for the horizontal positioning of the bubble b) A conceptual drawing of the capacitive sensing array used to track the vertical position of the microbubble.

Reproduced with permission of the copyright owner. Further reproduction prohibited without permission.

microbubble. This microbubble will then be forced in the opposite direction of buoyancy using this dielectrophoretic force. The system has been simulated using the IntelliSuite™ FEA simulation package and has shown that the maximum dielectrophoretic force that can be generated is 1.66 nN. This is more than adequate to compensate for the 1.02 nN force created by the natural buoyancy of the bubble. With an actuation voltage of 255V, the bubble will be held still and the actuation of the DEP electrodes will control the positioning of the microbubble. A set of five capacitive sensing electrodes will be used to determine the vertical position of the microbubble. When the position of the microbubble ascends beyond the middle electrode the DEP electrodes will engage and gently push the bubble back towards the center. The capacitive sensing pairs can be tuned to monitor the capacitance change from 6.15 pF, when there is no microbubble, to 14.87pF when the microbubble is present. The combination of these two components of the microbubble stabilization module provides an extremely desirable trait for extreme pressure sensing applications; neither the DEP electrodes nor the capacitive sensing array experience deformation during operation. Therefore strain in the device is minimal, resulting in a large expected mean time before failure due to mechanical wear.

Reproduced with permission of the copyright owner. Further reproduction prohibited without permission.

CHAPTER 5

PHOTODETECTION

5.1 Motivation

The photodetection stage of the microsensor is the final transduction stage where the light pulses emitted by the sonoluminescence phenomenon are to be detected to generate an equivalent photo-current. The design of the photodetector depends on two factors: first is the material selection and the second is the quantum efficiency. The material selection will determine the quality of the photodetector. With the current MEMS fabrication technology there are limitations to the available materials that can be deposited. The two types of photodetectors that were investigated most extensively are

Reproduced with permission of the copyright owner. Further reproduction prohibited without permission.

cadmium sulphide (CdS) and profiled silicon photodetectors. The quantum efficiency of these sensors will ultimately determine how sensitive the sonoluminescent microsensor will be. This chapter will describe the possible materials used for blue light photodetection and describe the sensitivity model.

5.2 Photodetection

This final stage of the transduction process critical as it will determine the sensitivity as seen externally. A photodetector capable of high efficiency sensing of blue light will ensure that the majority of the photonic energy released by the sonoluminescence is transferred to an electrical signal, yielding a high sensitivity [17-20].

The physical principle by which photodetectors convert light into electricity is the photovoltaic effect. The photovoltaic effect is the physical process in which light is converted into a usable electric current. Light is composed of photons. These photons contain various amounts of energy corresponding to different wavelengths of light. When photons strike a photovoltaic material they are reflected, absorbed, or they may penetrate through. When a photon is absorbed, the energy of the photon is transferred to an electron in an atom of the photodetector (which is actually a semiconductor). The injection of energy from the photon allows the electron to escape from stable orbit associated with a specific atom to form an electron hole pair. The electron becomes a free carrier and participates as part of the current in an electrical circuit [17-20].

5.2.1 Cadmium Sulphide Type Photodetectors

One of the materials that were investigated is cadmium sulphide (CdS). As shown in [20], the CdS type photodetectors can detect the wavelengths in the 400-500 nm range. This material was chosen as a candidate for the photodetectors due to its good

Reproduced with permission of the copyright owner. Further reproduction prohibited without permission.

performance within the spectral range. The good spectral performance comes from the fact that sonoluminescence emits high quantities of blue light, where the wavelength is approximately 460nm. Cadmium sulfide has a maximum cut off wavelength of 512 nm for spectral sensitivity. This photodetector is a good candidate for the purpose of blue light detection. However, this type of photodetector does have some limitations. The first limitation is that the material is fairly complicated to deposit using the current MEMS technology due to the vapor pressure associated with the cadmium tending to foul vacuum systems. The process for incorporating a non-standard MEMS material deposition and etching techniques is time consuming. The quantum efficiency of the CdS photodetector is approximately 30% efficient for a wavelength of 480 nm. Compared to the quantum efficiencies of other commercially available photodetectors such as gallium arsenide (GaAs at 18%) [20]. CdS provides a higher optically generated current.

5.2.2 Profiled Silicon Type Photodetector

Profiled silicon [17] photodetectors were another design considered. Profiled silicon photodetectors can be used to detect the emitted pulses of light due to its excellent photoconductivity over a wide range of frequencies, including blue light. This photodetector can be used as sonoluminescence emits light in the region of highest quantum efficiency. Profiled silicon has a maximum cut off wavelength of 390 nm.

Reproduced with permission of the copyright owner. Further reproduction prohibited without permission.

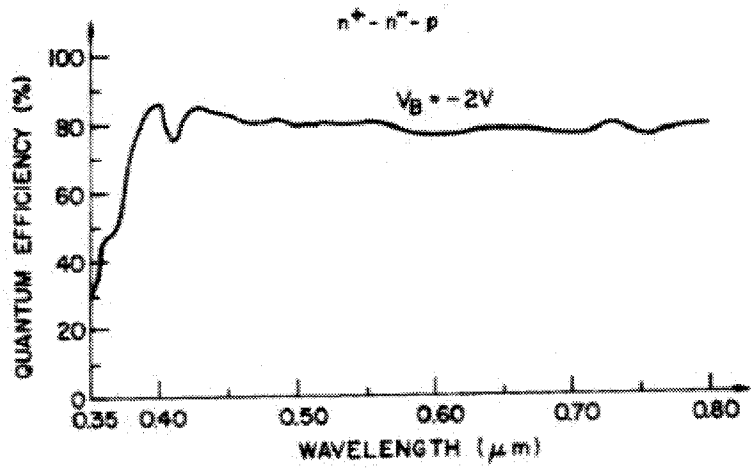

Figure 19. Quantum efficiency as a function of wavelength for a profiled silicon photodetector. Courtesy S. Chamberlain.

This type of photodetector has been shown in [17] to have a quantum efficiency of 80% or greater throughout the entire visible spectrum. With this high level of quantum efficiency this will guarantee the generation of electron-hole pairs for each incident photon, which will result in higher electric current. A characteristic graph showing the quantum efficiency of profiled silicon as a function of wavelength is shown in figure 19.

Fabrication of profiled silicon photodetectors are not plagued with the complications associated with other heavy metal based detectors. The fabrication requires two layers of ion implantation. The photodetector consists of three layers of doped silicon [17]. The first layer is n^+, the second is n^-, and the third is p type silicon. The tiered layering can be seen in Figure 20. Since the current MEMS fabrication facilities already implement high precision ion implantation to dope silicon, this type of photodetector is compatible with existing MEMS fabrication techniques and can draw from a large body of experience and knowledge for fabrication process details.

Reproduced with permission of the copyright owner. Further reproduction prohibited without permission.

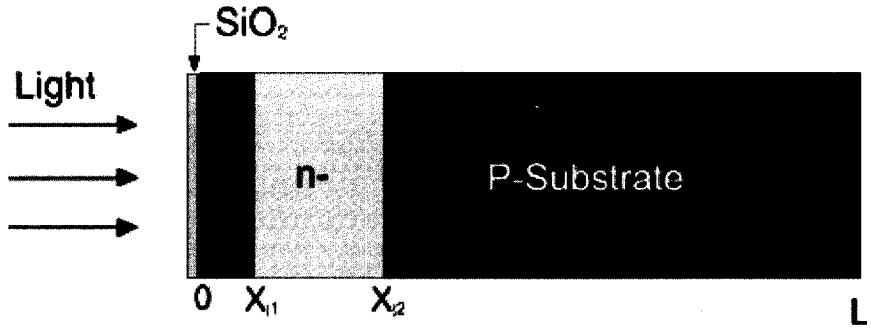

Figure 20. A profiled silicon photodetector.

5.3 Sensitivity Model

One important design parameter for a sensor is its sensitivity that quantifies the generated electrical signal per unit of external excitation during the transduction process. Optimizing the sensitivity is an important design factor. A sonoluminescing bubble emits 10^6 photons per acoustical cycle (per flash of light) for driving acoustical amplitudes of 1.2 atm and above. Consequently, sonoluminescence will produce the same number of photons with every pulse of light regardless of the amplitude of the exciting signal.

To determine the sensitivity, at first the amount of optical power generated by one photon of blue light with a wavelength of 480 nm has been calculated following the optical energy equation as expressed below:

$$E = \frac{hc}{\lambda} \tag{15}$$

Where, h is planks constant, c is the speed of light and λ is the wavelength. From equation (15), the optical power associated with a photon at 480 nm wavelength can be calculated as 4.14×10^{-21} J. Therefore, 10^6 photons will produce 4.14×10^{-15} J of optical power. To calculate the amount of optical power in J/s, the average of 100 picoseconds was used as the refresh time of a sonoluminescing bubble [2, 7-9]. The optical power of 4.14 mW, can be calculated using the following formula:

Reproduced with permission of the copyright owner. Further reproduction prohibited without permission.

$$P(opt) = \frac{Energy}{Time} \tag{16}$$

From [21], it is now possible to calculate the resulting optically generated photocurrent for the profiled silicon photodetector. The formula for optically generated photocurrent of an n^+-n^--p type junction is described as [21]:

$$I = (1-R)(1-e^{-\alpha d})\frac{qP}{hv} \tag{17}$$

Where, R is the reflection coefficient, α is the absorption coefficient, d is the depth of the absorption region, q is the charge of an electron, h is Plancks constant, P is the optical power in Watts and v is the frequency of the incident light wave [21]. This equation takes into account the losses that occur during refraction and during absorption. Following (17) a photocurrent of 624 μA per flash of light (each bubble collapse) has been calculated when the peak amplitude of the incident ultrasonic wave is 1.2 atm. Thus, a sensitivity has been determined to be 624 μA/1.2 atm or 520 μA/atm.

5.4 Conclusions

This chapter develops a sensitivity model for the microsensor and describes the selection of a profiled silicon photodetector as the final transduction stage for the proposed microsensor. A sensitivity of 520 μA/atm was calculated when the maximum amplitude of the incident ultrasonic wave is 1.2 atm or higher including losses due to refraction and absorption. This is a suitably high current that can be easily amplified by existing microelectronic circuitry.

Reproduced with permission of the copyright owner. Further reproduction prohibited without permission.

CHAPTER 6

SENSOR FABRICATION

6.1 Motivation

This chapter describes the details of the developed fabrication process sequences to fabricate the microsensor. The entire process sequence has been divided into eight main steps. For each major step, a cross-sectional drawing is provided along with a 3-D model of the structure obtained after simulating the associated process steps in IntelliSuite™. The process steps were checked with the foundry process steps available in the Univeristy of Alberta Nanofabrication Laboratory and consultation was made with the University of Alberta Nanofabrication facility for process compatibility. The microsensor can be fabricated and tested once the necessary funding is available.

Reproduced with permission of the copyright owner. Further reproduction prohibited without permission.

6.2 Microfabrication

Microfabrication, is the technique of sequential deposition, patterning and etching of thin film materials to construct a 3-D geometry of a microstructure. Major MEMS fabrication techniques can be categorized as either surface micromachining, bulk micromachining or wafer bonding. The developed process steps to fabricate the device are a combination of both surface and bulk micromachining techniques. Below is a brief discussion on different techniques that have been used to fabricate the device.

6.2.1 Ion Implantation

Ion implantation is a process where a particle accelerator injects a beam of dopant atoms directly into a wafer. These atoms are able to penetrate the surface of the wafer and may be embedded at a defined depth. The beam is scanned across the surface as the wafer is rotated to achieve a uniform dopant distribution [14]. By monitoring the ion current the doping can be accurately controlled. The amount of energy that is carried by the ion will determine within a narrow tolerance how deep the implanted dopant atom is inserted within the substrate. Photoresist and other dielectric films such as silicon nitride can be used to mask selected areas of a wafer from ion implantation by absorbing the energy from the ion preventing it from embedding into the substrate. This allows for selective doping of different regions of a given wafer [14, 21].

6.2.2 Physical Vapor Deposition (PVD)

Physical vapor deposition is an umbrella term covering two similar methods of material deposition; evaporation and sputtering. For evaporation, the metal that is to be deposited is heated in a crucible by an incident electron beam. The flux of vapor atoms created by this heating is allowed to reach the wafer. This type of deposition must be

Reproduced with permission of the copyright owner. Further reproduction prohibited without permission.

carried out in a high-vacuum chamber to ensure the mean free path is long enough to ensure delivery of the atoms to the substrate. Evaporation with an electron beam is also quite directional, allowing for sidewall coverage [14, 21]. Sidewall coverage can also be increased by rotating the wafer to allow for better deposition.

For sputtering, the process uses chemically inert atoms to facilitate the process. Chemically inert atoms, typically argon, are ionized into plasma. These ions are then accelerated onto a source target using an electric field. When the ions hit the target, atoms from the target are knocked loose and are allowed to reach the wafer. This process is less directional than evaporation but it can yield higher deposition rates. Because of this high deposition rate, it is often used for metallic deposition such as Aluminum or Chromium [14, 21].

6.2.3 Chemical Vapor Deposition (CVD)

Chemical vapor deposition is a method where precursor materials are placed into a heated furnace. A chemical reaction occurs on the surface of the wafer which results in a deposition. CVDs that are performed in a low pressure environment are classified as low pressure chemical vapor deposition (LPCVD). LPCVDs typically involve the use of an inert diluent gas in addition to the reactive species. The temperatures of these LPCVD processes can reach up to 850°C. These temperatures are too high to be used with wafers that have previously been subject to metallic depositions such as gold or aluminium. The need for careful process planning is needed when the design requires an LPCVD deposition [14, 21].

Reproduced with permission of the copyright owner. Further reproduction prohibited without permission.

6.2.4 Spin Casting

Thin films can be deposited in the form of a solution by a technique called spin casting. The material to be deposited in this manner is usually a polymer or a photoresist. The solution is applied at the center of the wafer and the wafer rotated at a high speed. During rotation of the wafer, the solution will spread itself across the surface of the wafer with a uniform thickness due to the centrifugal forces. After the spinning process is complete, a curing stage is required to remove the excess liquids in the solution solidify the newly deposited layer. This is the standard process for the application of most photoresists prior to the photolithography stage [14, 21].

6.2.5 Optical Lithography

To obtain a pattern on a photoresist, photolithography is a standard process. This process utilizes a mask, typically made from chromium on glass to selectively expose a wafer coated in photoresist to a light source. Photoresists exposed to light undergo a one way curing reaction, where polymer chains within the resist crosslink, creating a much more durable material then the unexposed resist. The photomask contains the pattern to be transferred to the photoresist. The mask is placed in contact with the photoresist and a UV light for example is directed through the transparent regions of the mask until the photoresist is cured. A photoresist stripping stage is required to remove the non-exposed photoresist so the subsequent layers can be etched [14, 21].

6.2.6 Deep Reactive Ion Etching

Deep reactive ion etching (DRIE) is a relatively new process. This process takes advantage of the side effects of glow discharge (plasma), the tendency to create polymeric species by chemical cross linking [14]. During this process alternating steps of

Reproduced with permission of the copyright owner. Further reproduction prohibited without permission.

reactive-ion etching and polymer deposition are used. During the etch process the polymer is rapidly removed from the bottom of the feature but remains along the sidewall. This protects the sidewall from the etchant. As a result deep sidewall etching can be created where the top of the hole does not get wider. This type of etching is used where high aspect ratios are required [14, 21].

6.2.7 Chemical Mechanical Polishing

Chemical mechanical polishing (CMP) is a process where a wafer is pressed against a rotating polishing wheel and an abrasive slurry is applied. This slurry is a mix of corrosive and abrasive particles which assists in the removal of the material. This technique can be used to create extremely flat surfaces. This is useful between deposition processes to keep the layers extremely flat and to finish surfaces prior to bonding [14, 21, 23].

6.2.8 Direct Wafer Bonding

Wafer bonding is the process of permanently joining two wafers together to create a stacked wafer. Direct bonding of silicon wafers can be accomplished by first cleaning and hydrating (wetting) the surfaces. They must be smooth and particulate free. Particulates or contaminates create gaps that can weaken the bond during the bonding process. The bonding process requires the surfaces to be contacted after cleaned wafers are pressed together and heated to fuse the wafers together [14, 21, 24].

6.3 Microsensor Fabrication

The fabrication process for the proposed micro-sensor consists of eight major steps.

Reproduced with permission of the copyright owner. Further reproduction prohibited without permission.

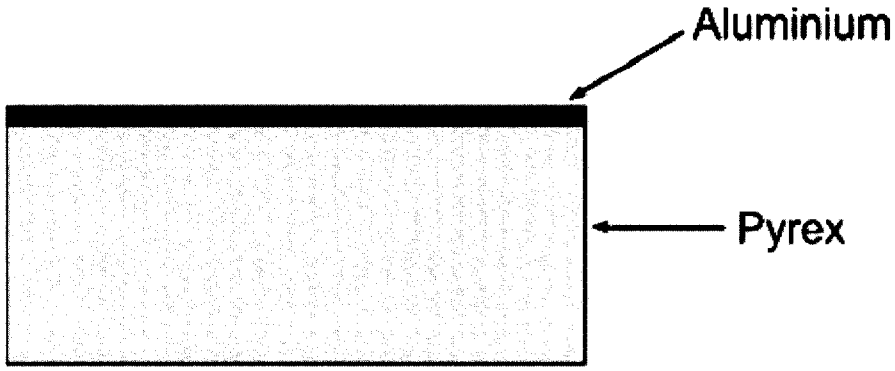

Figure 21. DC Magnetron sputtered aluminium deposited atop a Pyrex substrate.

Step 1: The fabrication begins with a 500 μm thick Pyrex 7740 glass substrate which is used as the base of the microsensor. A 175 nm thick layer of aluminum is deposited on the top side of the substrate using a low power DC-magnetron sputtering process as shown in Figure 21. This sputtering process uses a cathode power of 250W and an ambient chamber pressure of 5 mTorr. AZ P4400 photoresist is then spun on top of the wafer. The spin process is conducted using a vacuum chuck to secure the wafer. The wafer is then spun at 600 rpm for 10 seconds while the AZ P4400 photoresist is applied at the center of the wafer. The secured wafer is then spun at 2800 rpm to thin the layer to 3.3 μm then baked on a hot plate at 110°C for 3 minutes and 20 seconds. Next, optical lithography is performed to transfer the mask pattern onto the photoresist. The photoresist layer is then developed using AZ 400K solvent. The wafer is then rinsed with de-ionized (DI) water and dried using compressed nitrogen. The aluminum is then wet etched at 25°C using a solution of phosphoric acid. A subsequent photoresist ashing step is required to remove any residual photoresist. This is done by using a 100% O_2 plasma flow at 400 mTorr for 20 minutes.

Step 2: A Piranha clean is conducted prior to depositing a layer of 2 μm thick phosphosilicate glass (PSG) using a Low Pressure Chemical Vapor Deposition (LPCVD)

Reproduced with permission of the copyright owner. Further reproduction prohibited without permission.

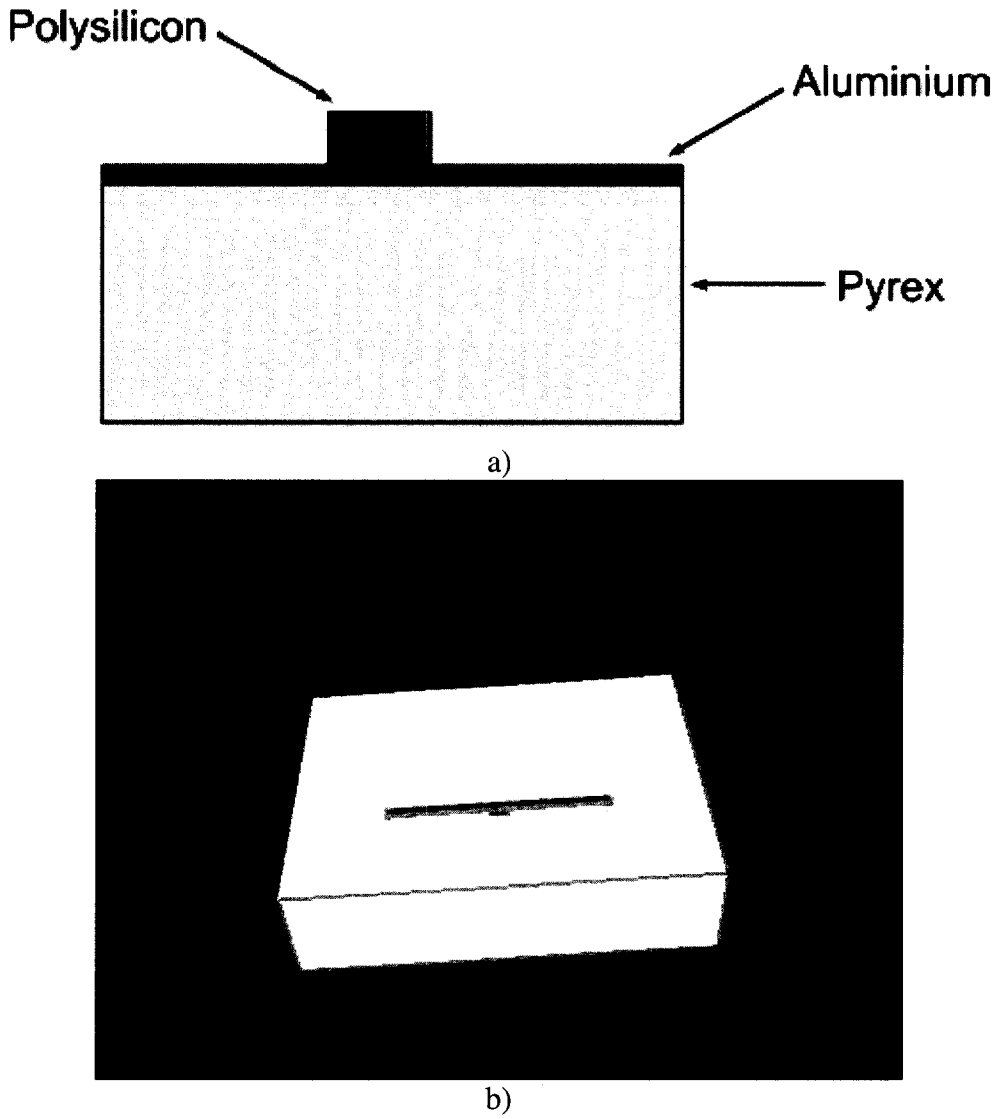

Figure 22. (a) A conceptual cross-sectional diagram of the microheater. (b) IntelliSuite™ generated 3-D model after simulating process steps for the microheater.

method atop the aluminum layer. This LPCVD process is conducted at a temperature of 400°C and a chamber pressure of 300 mTorr. The PSG layer is patterned using the AZ P4400 photoresist technique and etched using the Bosch ICP RIE process. The ICP RIE etch process is done using SF_6 with a chamber pressure of 150 mTorr. Afterwards the 0.5 μm thick polysilicon microheater as shown in figure 22 (a), has been deposited by an

Reproduced with permission of the copyright owner. Further reproduction prohibited without permission.

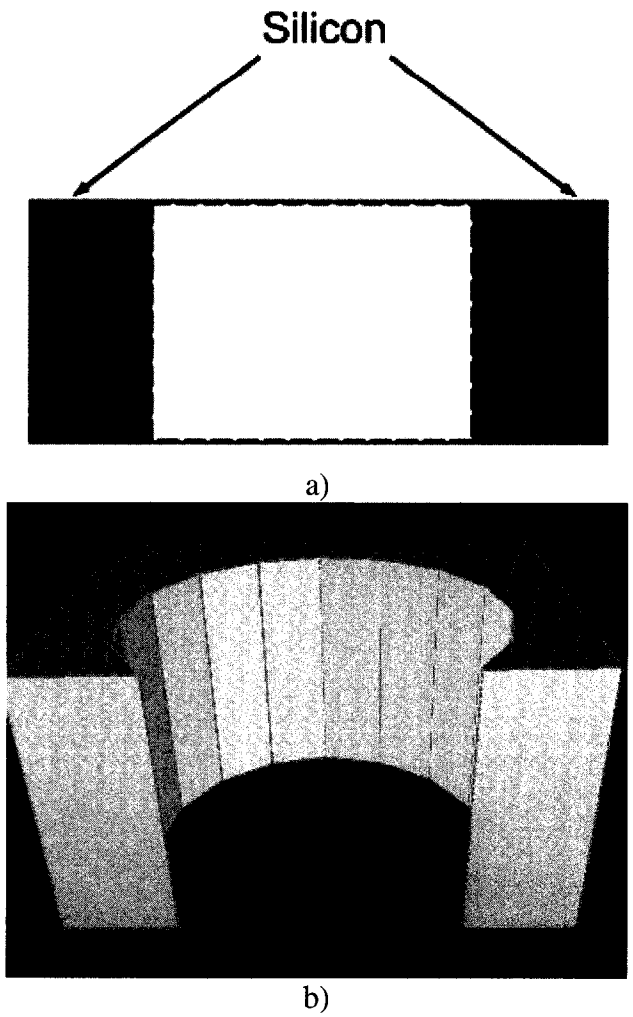

Figure 23. (a) A conceptual cross-sectional diagram of the side walls. (b) IntelliSuite™ generated 3-D model after simulating process steps for the sidewalls.

LPCVD process. The standard LPCVD process is modified to ensure low stress in the thin film by increasing the temperature to 588°C with a chamber pressure of 110 mTorr. The polysilicon has been patterned with AZ P4400 and etched using $HN0_3$ at 25°C to realize the microheater geometry [24, 25].

Step 3: To create the 150 μm wide cylindrical sidewall shown as in Figure 23 a separate four inch prime silicon wafer is to be patterned using AZ P4400 photoresist and etched using the same Bosch ICP RIE techniques. To thin the wafer to 110 μm, a combination of

Reproduced with permission of the copyright owner. Further reproduction prohibited without permission.

surface micromachining and CMP (chemical-mechanical polishing) is to be used [24, 25]. For surface micromachining the substrate is held on a rotating pad and pressed against a second large rotating grindstone. For the grinding, a slurry containing small very hard particles of diamond or boron oxide has been used [24, 25].

Step 4: To create the capacitive sensing electrodes, a third wafer is used. An ultra uniform SOI wafer can be used to ensure that the height difference in the capacitive sensing electrodes will be minimal. The thickness uniformity can be as uniform as ±0.15 μm across the wafer [24, 25]. Five capacitive sensing electrodes shown in figure 24 will be fabricated by first depositing a 10 μm thick layer of LPCVD (low-stress) silicon, then thermally growing 5 μm of SiO_2 at a temperature of 1200°C as an insulating layer. This process is repeated five times to create the capacitive sensing array. However, an annealing stage is required between each subsequent layer to reduce any residual stress in the silicon or the insulating layer. Patterning of the silicon is done by using AZ P4400 and then the silicon is boron doped with a dopant concentration of $8x10^{19}$ atom/cc in a in a chamber with a temperature and pressure of 1175°C and 1 atm respectively.

Step 5: The top of the micro-chamber as shown in figure 25 is to be fabricated on the same four inch wafer used to create the sidewall surrounding the polysilicon microheater. A section of the four inch wafer will be patterned using AZ P4400 photoresist and boron doped using the same boron doping technique with a dopant concentration of $8x10^{19}$ atom/cc. Two fluid canals will be created using Bosch ICP RIE technique to allow for the microchamber to be filled with water.

Reproduced with permission of the copyright owner. Further reproduction prohibited without permission.

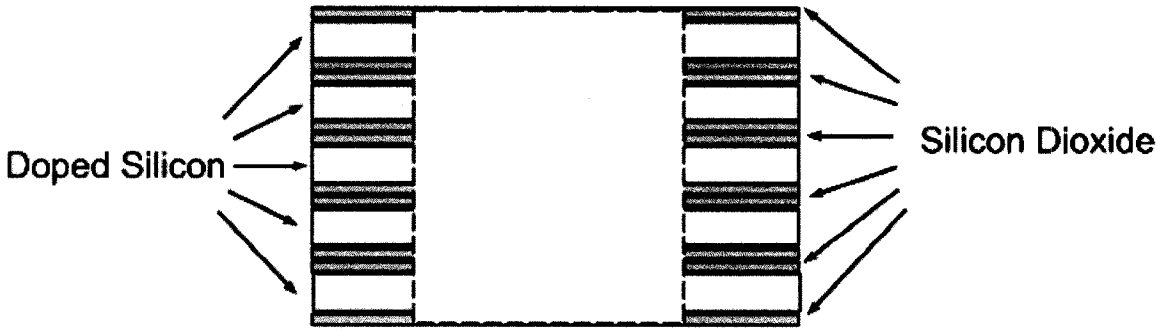

a)

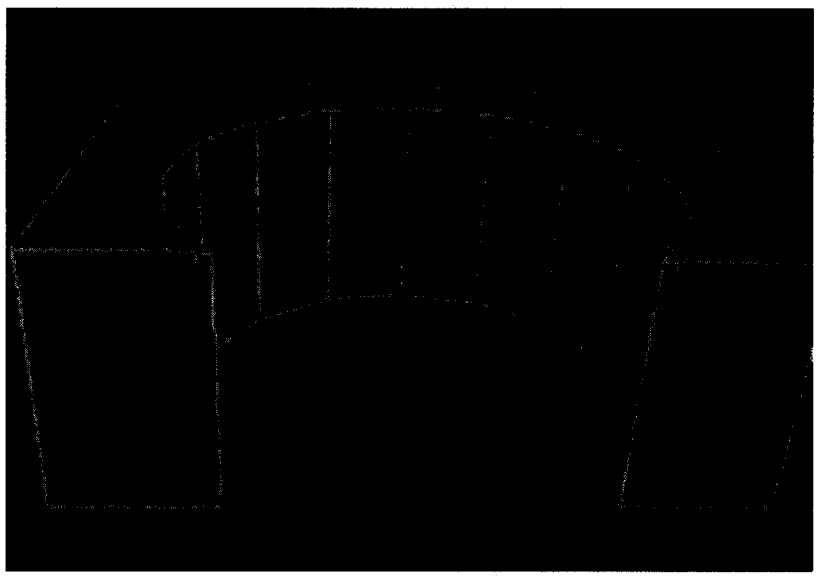

b)

Figure 24. (a) A conceptual cross-sectional diagram of the capacitive sensor array. (b) IntelliSuite™ generated 3-D model after simulating the process steps for the capacitive sensing array.

Reproduced with permission of the copyright owner. Further reproduction prohibited without permission.

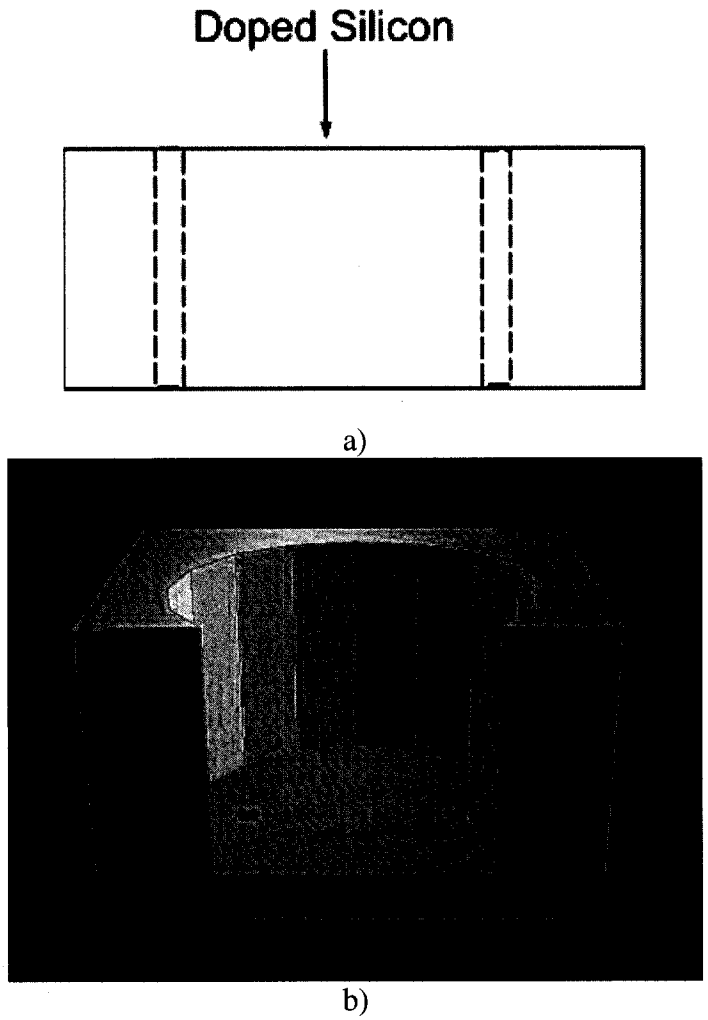

Figure 25. (a) A conceptual cross-sectional diagram of the top lid. (b) IntelliSuite™ generated 3-D model for the top lid of the microstructure.

Step 6: To create the photodetector, a four inch wafer of 500 μm thick p-type substrate wafer is to be used. By using the process steps described in [17], the profiled silicon photodetector can be realized. This photodetector is next to be bonded to the bottom of the Pyrex 7740 substrate. Silicon bonding can be done in air with an ambient pressure of 1.0 atm and under the constraint that no organic materials are allowed in the bonding chamber [24, 25]. To prepare the remaining pieces for bonding a Piranha clean will be used to remove any remaining organics. Then to finalize the realization of the micro-

Reproduced with permission of the copyright owner. Further reproduction prohibited without permission.

chamber, SU-8 photoresist can be used as an epoxy to bond all the pre-fabricated pieces. SU-8 is an epoxy commonly used as a photoresist. Using a vacuum chuck to secure wafers, SU-8 photoresist is then applied. The chuck spins at 4000 rpm for 40 seconds while SU-8 is applied to a thickness of 2 μm. The first piece to be bonded is the sidewall surrounding the microheater as shown in figure 26. The Pyrex 7740 wafer is secured using the vacuum chuck and SU-8 is spun around the microheater. The sidewall piece is then optically aligned and pushed down into the photoresist. The two pieces will then be soft-baked at 65°C for 60 seconds and then at 120°C for 120 seconds to cure the SU-8. To ensure the bond is complete, the two pieces are then hard-baked to ensure the SU-8 is completely cured. Hard-baking is done first at 65°C for 60 seconds and then at 95°C for 60 seconds [24, 25]. To remove any unwanted SU-8 around the microheater and within the microchamber after the bonding procedure Dynasol 165 is used [24, 25].

Step 7: The five capacitive sensing array is next to be bonded to the structure and finally the top lid of the microchamber will be bonded both using the same SU-8 epoxy technique as shown in Figure 27 and Figure 28. The photodetector will be direct wafer bonded to bottom of the Pyrex substrate. The benefit for using this epoxy technique is to ensure that low temperatures are used to finalize the micro-chamber as high temperatures will induce diffusion in the photodetector layer of the micro-sensor. This epoxy technique guarantees that the photodetection module will not be held in an environment where high temperatures are required for extended periods of time. By keeping the temperatures to a minimum, minimal dopant diffusion can occur in the photodetector.

Reproduced with permission of the copyright owner. Further reproduction prohibited without permission.

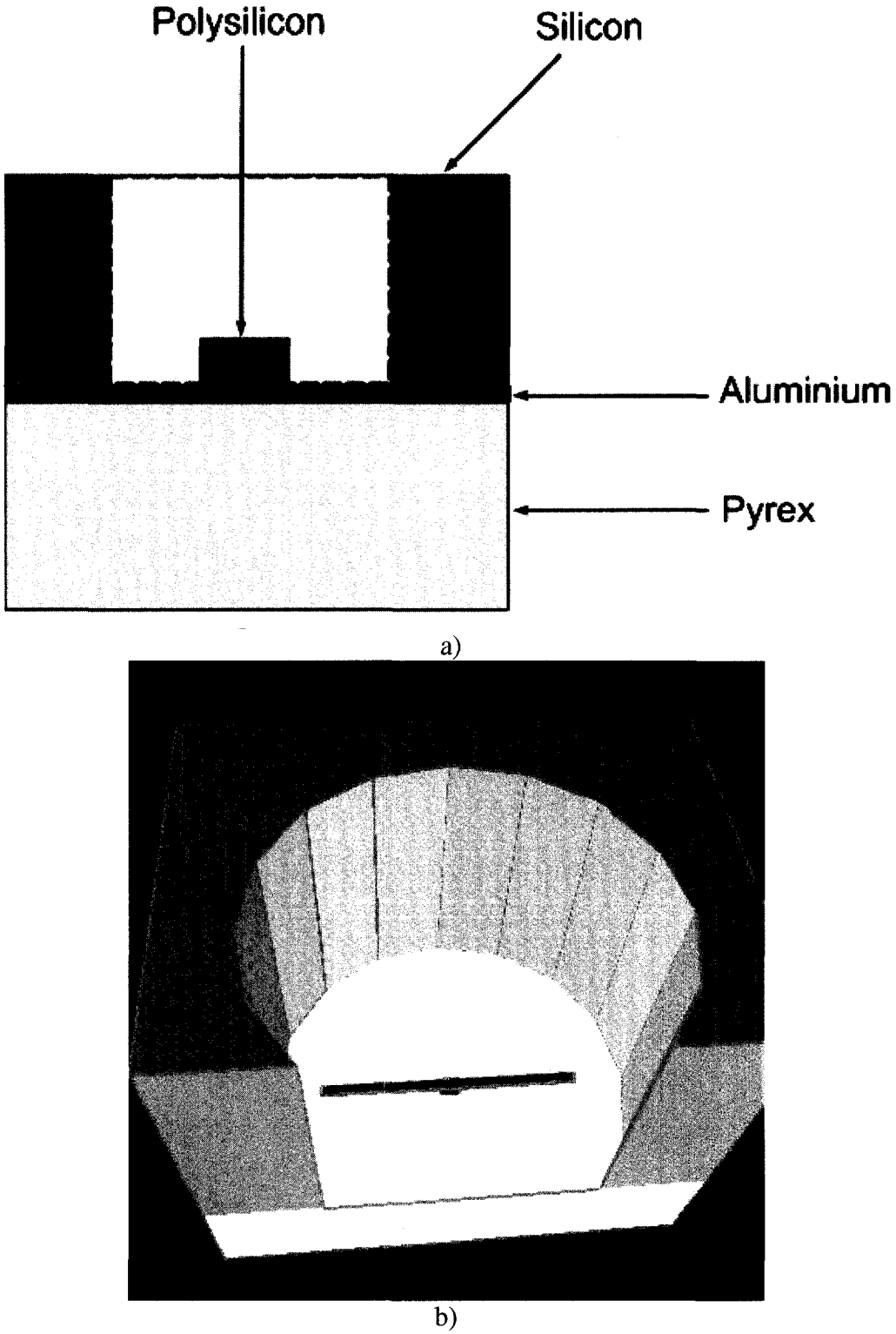

Figure 26. (a) A conceptual cross-sectional diagram of the bonded sidewalls around the microheater. (b) IntelliSuite™ generated 3-D model after simulating process steps for bonding the sidewalls around the microheater.

Reproduced with permission of the copyright owner. Further reproduction prohibited without permission.

Step 8: The final step is the bonding of the photodetector to the bottom of the Pyrex substrate as shown in figure 29 and figure 30. The photodetector will be direct wafer bonded. The low temperature at which this process can be achieved will allow for minimal dopant diffusion within the photodetector.

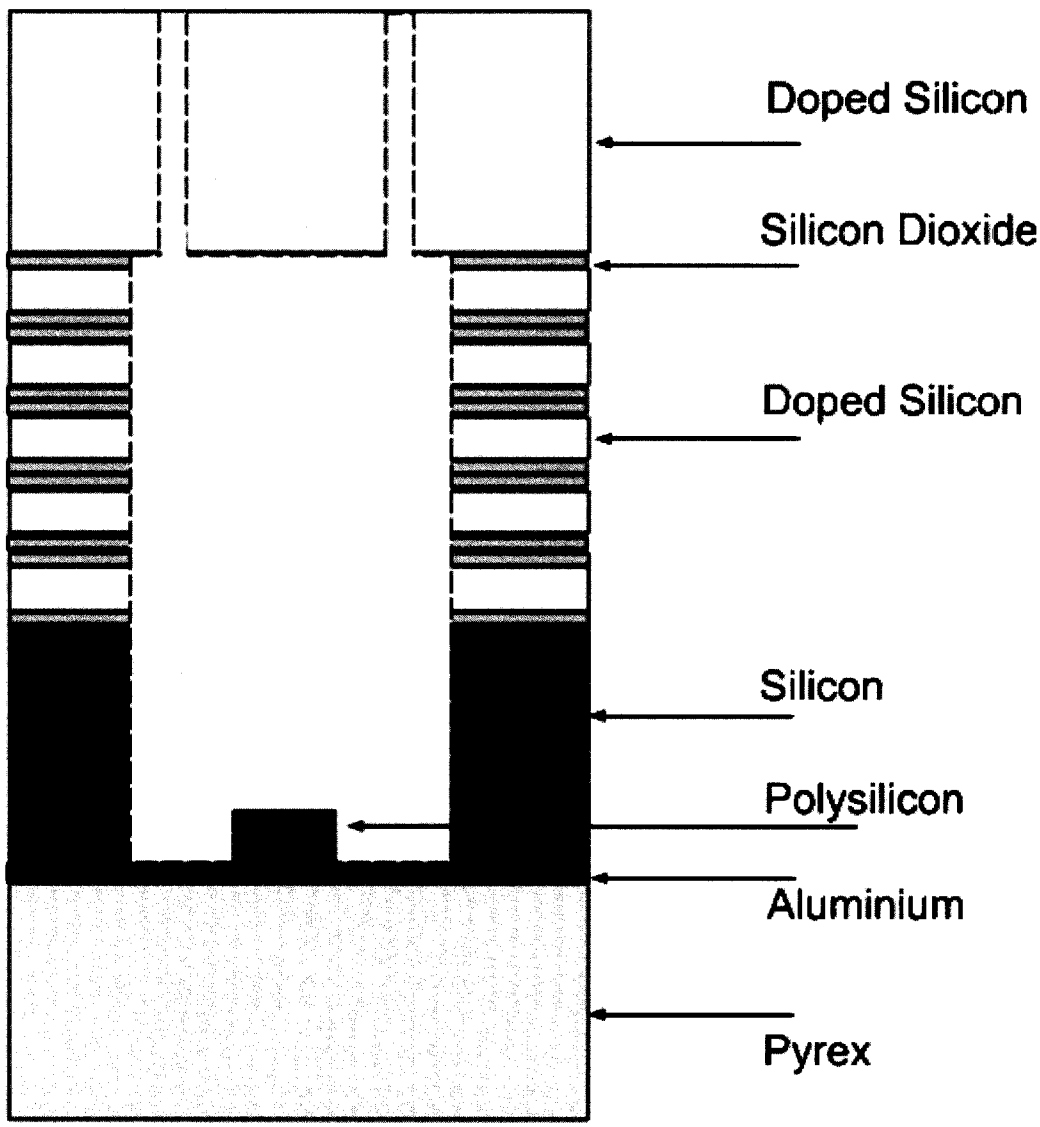

Figure 27. A conceptual cross-sectional diagram of the completed microchamber after step 7.

Reproduced with permission of the copyright owner. Further reproduction prohibited without permission.

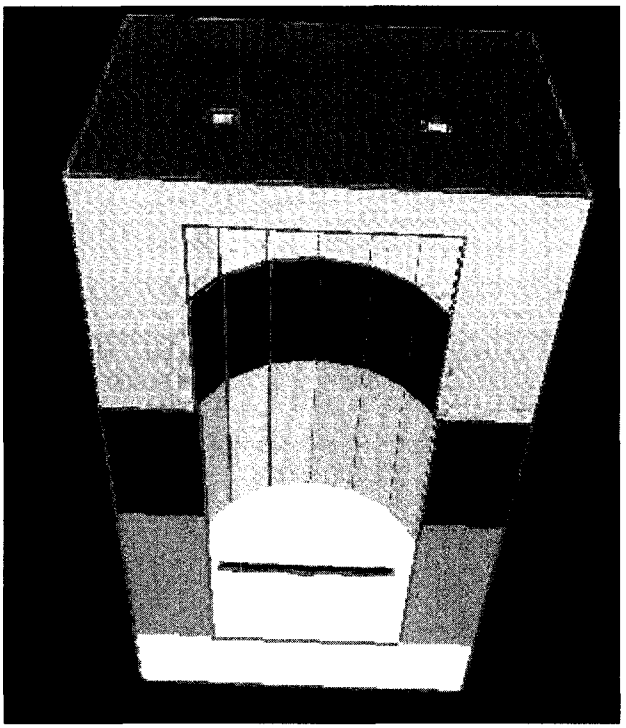

Figure 28. An IntelliSuite™ 3-D simulated model of the completed microstructure after step 7.

Reproduced with permission of the copyright owner. Further reproduction prohibited without permission.

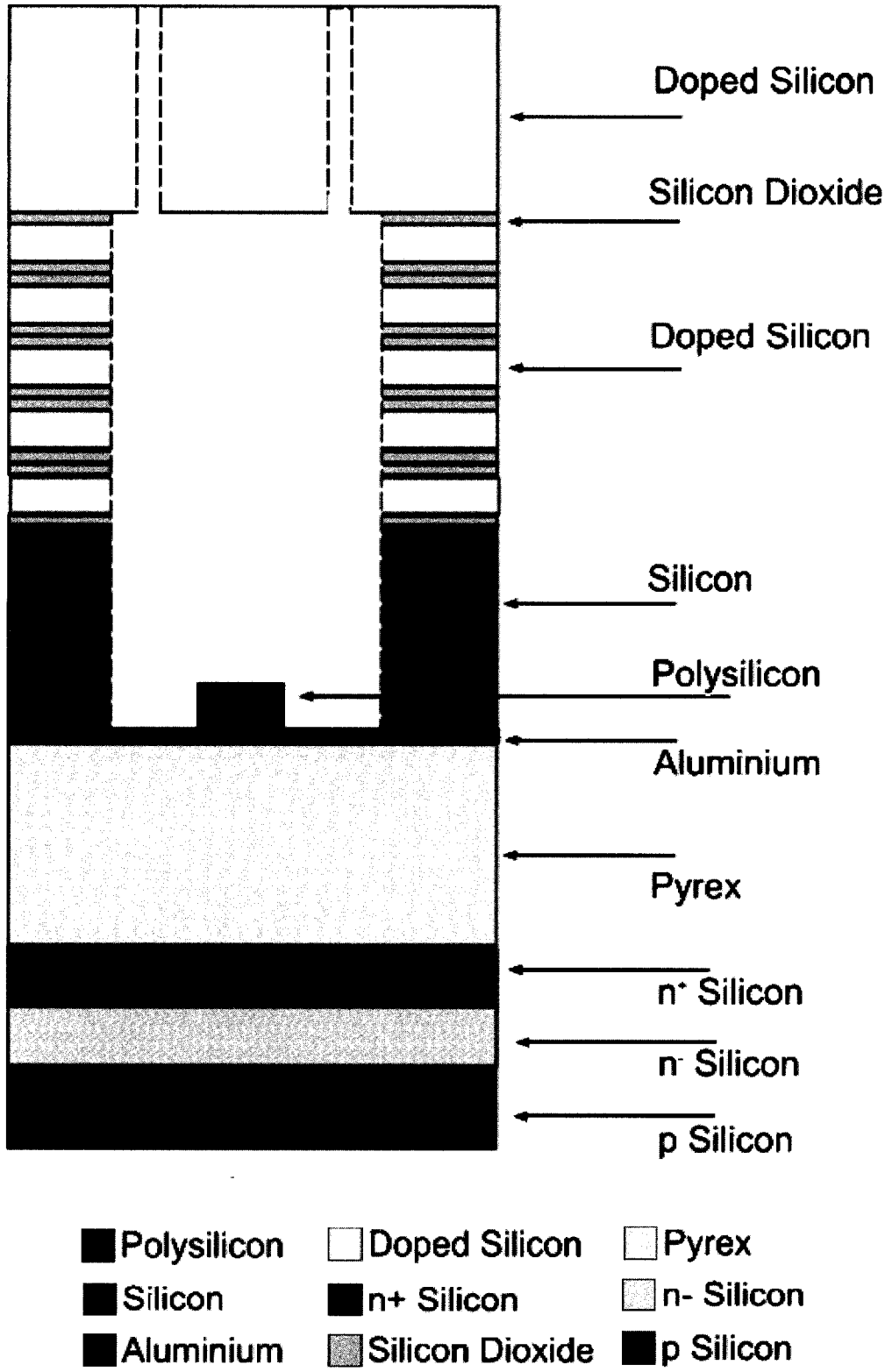

Figure 29. A conceptual cross-sectional diagram of the complete microsensor with the photodetector bonded to the bottom.

Reproduced with permission of the copyright owner. Further reproduction prohibited without permission.

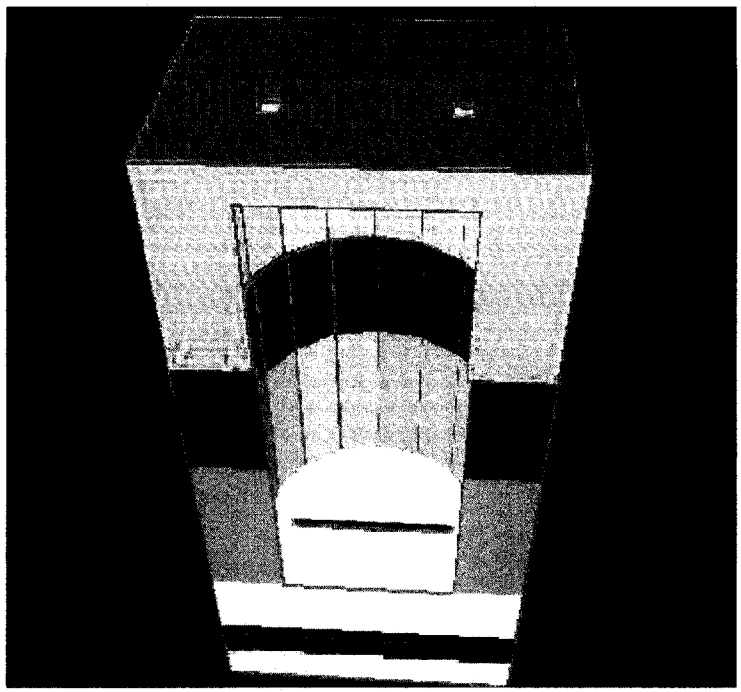

Figure 30. An IntelliSuite™ 3-D simulated model of the completed microstructure after bonding the photodetector to the bottom of the microsensor.

6.4 Conclusions

A brief introduction to the state-of-the-art MEMS fabrication techniques used to fabricate the microsensor has been presented. A custom fabrication process table has been developed and verified for compatibility with University of Alberta Nanofabrication Laboratory. The developed custom fabricated process table has been simulated using IntelliSuite™ simulation package to generate a 3-D model of the sensor geometry. The developed models have been found to be in excellent agreement with the design requirements.

Reproduced with permission of the copyright owner. Further reproduction prohibited without permission.

CHAPTER 7

CONCLUSIONS

7.1 Design Summary

A novel MEMS ultrasonic microsensor that exploits the single bubble sonoluminescence (SBSL) phenomenon has been developed. The microsensor has a cylindrical geometry with a height of 300 μm. The inner diameter of the microchamber is 150 μm. This is large enough to contain a floating microbubble of 5 μm in radius. The three main modules of the microsensor are the microbubble generation module, the microbubble stabilization module and the photodetection module.

The microbubble generation module is capable of attaining a temperature of up to 150°C. The required temperature for bubble nucleation on this microheater is 136°C. The microheater is fabricated using a low-stress LPCVD deposited polysilicon. The

Reproduced with permission of the copyright owner. Further reproduction prohibited without permission.

dimensions of the microheater are 100 μm x 4 μm x 0.5 μm. There are a couple of the inherent qualities for this type of microbubble generation unit. The first is that the microheater can be electrostatically actuated in the event that the bubble becomes stuck to the microheater surface. The second is the ability to nucleate a microbubble consistently with only 0.4 mA. The total power consumed by the microheater to nucleate a bubble is 1.183 mW.

The microbubble stabilization unit is comprised of two modules. The first is the electrokinetic bubble manipulation electrodes. The second is an array of five capacitive sensors. These sensors will monitor the elevation of the bubble. Dielectrophoresis has been used to stabilize and manipulate the microbubble within the microchamber. Dielectrophoresis creates a dipole in the target particle within a gradient electric field. The dipole within the microbubble, the particle, reacts with the gradient electric field. The electric field produces a net force on the microbubble. This net force moves the bubble in the direction of the force. The electromagnetic field simultaneously positions the microbubble into the horizontal center. FEA simulation results using IntelliSuite™ for microbubble stabilization are in excellent agreement with calculated results. The calculated force of buoyancy is 1.02 nN. The maximum force applicable by the dielectrophoresis electrodes is 1.66 nN. This is more than enough force to reposition the bubble back to the center of the microchamber. The capacitive sensing array is fabricated using doped polysilicon between layers of silicon nitride. The minimum capacitance for a single pair of polysilicon capacitive plates is 6.15 pF, and the maximum capacitance is 14.87 pF. This capacitance change can be sensed using suitable sensing circuitry. The capacitive array detects the vertical motion of the bubble. When the bubble passes above

Reproduced with permission of the copyright owner. Further reproduction prohibited without permission.

the middle pair of electrodes the capacitive sensors will activate the control to active the dielectrophoresis electrodes. The electrodes will push the bubble back into the vertical center.

The profiled silicon photodetection module converts light emitted by sonoluminescence into an electrical current. The photodetector is created by doping selected layers of a silicon wafer. The detector has a high quantum efficiency of 80% throughout the entire visible spectrum even at 480 nm, the wavelength of blue light. The amount of current produced over the time span of one acoustic cycle is 624 μA.

The sensitivity of the entire system has been calculated to be 520 μA/atm, regardless of the amplitude of the incident ultrasonic wave as long as the acoustical drive pressure is above 1.2 atm.

A detailed fabrication scheme for the photodetector has been developed. These techniques are currently in use at the University of Alberta Nanofabrication Laboratory. These processes can be found and examined using their online database. The fabrication of this device was done mainly with polysilicon and silicon wafers. This design will lower the cost by eliminating the need to deposit different foreign materials as well as eliminate the need for designing a new process to deposit these materials.

The overall design of the sonoluminescent ultrasonic microsensor has some benefits over the conventional types of ultrasonic sensors. Conventional ultrasonic sensors inherently have no internal amplification during the transduction mechanism. Sonoluminescence has an amplification factor of thirteen related to the ultrasonic drive pressure. This occurs during the conversion of sound into light. The microsensor also contains no mechanical or vibrating diaphragms. Since this microsensor does not contain

Reproduced with permission of the copyright owner. Further reproduction prohibited without permission.

any vibrating diaphragm it can not be affected by the pull-in phenomenon. Due to the absence of a deformable mechanical diaphragm or plate, the sensor is free of any stress related effects associated with capacitive or piezoresistive type MEMS ultrasonic sensors.

7.2 Industry Applications

Due to the specific requirements for sonoluminescence, the sensor is expected to be applicable to high pressure acoustical field sensing where conventional sensors are not suitable for their geometrical limitations. Sensors used for seismic identification, similar to what archaeologists use to detect fossils underground, or for ultrasonic density testing require high ultrasonic drive pressures. These high drive pressures are suitable to guarantee the generation of sonoluminescence. For the automotive industry, a high amplitude ultrasonic emitter could be mounted onto an automobile, whereby the sonoluminescent ultrasonic sensor could be used in automotive collision detection system.

Reproduced with permission of the copyright owner. Further reproduction prohibited without permission.

REFERENCES

[1] I. Ladabaum, X. C. Jin, H. T. Soh, A. Atalar, and B. T. Khuri-Yakub, "Surface Micromachined Capacitive Ultrasonic Transducers", *IEEE Trans. Ultrasonics, Ferrorelectrics and Frequency Control*, vol. 45, no. 3, pp. 678-690, May, 1998.

[2] M. P. Brenner, "Single-Bubble Sonoluminescence", *Rev. Modern Phys.* vol. 74, no. 2, pp. 426-472, Apr. 2002.

[3] F. Akasheh, T. Myers, J. D. Fraiser, S. Bose, "Development of Piezoelectric Micromachined Ultrasonic Transducers", *Sensors and Actuators A III*, vol. 111, no.3, pp. 275-278, Nov. 2004.

[4] P. Mattila, J. Stor-Pellinen, J. Ignatius, J. Hietanen, and M. Luukkala, "Capacitive Ultrasonic Transducer with Net Backplate", *Journal of Measurement Science and Technology*, vol. 11, no. 8, pp. 1119-1125, Aug. 2000.

[5] A. Caronti, G. Caliano, A. Iula and M. Pappalardo, "An Accurate Model of Capacitive Micromachined Ultrasonic Transducers", *IEEE Trans. Ultrasonics, Ferroelectrics and Frequency Control*, vol. 49, no. 2, pp. 159–168, Feb. 2002.

[6] P. C. Hsu, C. H. Mastrangelo and K. D. Wise, "A High Density Polysilicon Diaphragm Condenser Microphone", in *Technical Digest of IEEE 11th International Conference on Micro Electro Mechanical Systems (MEMS)*, Heidelberg, Germany, 1998, pp. 580-585.

Reproduced with permission of the copyright owner. Further reproduction prohibited without permission.

[7] S. Putterman "Sonoluminescence: Sound into Light", *Scientific American*, vol. 272, pp. 32-37, May, 1998.

[8] J. Holzfuss, M. Ruggerber "Micromanipulation of Sonoluminescing Bubbles", *Phys. Rev. E* , vol. 69, no. 5, pp, 056304-1-056304-8, 2004.

[9] S. Putterman "Sonoluminescence: The Star in a Jar", *Physics World*, vol. 11, pp. 38-42, May, 1998.

[10] E. R. Lee, *Microdrop Generation.* Florida: CRC Press Boca Raton, 2005, pp. 43-54.

[11] R. B. Maxwell, A. L. Gerhardt, "A Microbubble-Powered Bioparticle Actuator", *Journal of MEMS*, vol. 12, no. 5, pp. 630-641, Oct. 2003.

[12] L. Lin, "Microscale Thermal Bubble Formation: Thermophysical Phenomena and Applications", *Microscale Thermophysical Engineering*, vol. 2, no. 2, pp. 71-85, May, 1985.

[13] M. P. Hughes, "AC Electrokinetics: Applications for Nanotechnology", *Journal of Nanotechnology*, vol. 11, no. 2, pp. 124-132, Jun. 2000.

[14] S. D. Senturia, *Microsystems Design.* Kluwer Academic Publishers, MA: 2000 pp. 65-104.

[15] P. K. Wong, T. H. Wang, J. Deval, C. M. Ho, "Electrokinetics in Micro Devices for Biotechnology Applications", *IEEE Trans. on Mech.*, vol. 9, no. 2, pp. 366-377, Jun. 2004.

Reproduced with permission of the copyright owner. Further reproduction prohibited without permission.

[16] Intellisense Software Corporation, Woburn, MA, (2005) IntelliSuite™ Training Manual 8.0, pp.164-170.

[17] S. G Chamberlain, "Profiled Silicon Photodetector for Improved Blue Color and Visible Wavelength quantum Efficiency", in *Proc. International Electron Devices Meeting*, 1979, pp 137-140.

[18] B. V. Zeghbroeck, "Principles of Semiconductor Devices: Optoelectronic Devices", [Online]. Available: http://ece-www.colorado.edu/~bart/book/chap.

[19] W. A. Beckman, and J. A. Duffie, *Solar Engineering of Thermal Processes.* 2nd Ed. John Wiley and Sons, Inc., 1991, pp. 768-793.

[20] I. Robel, B. Bunker, and P. Kamat, "Single-Walled Carbon Nanotube- CdS Nanocomposites as Light-Harevesting Assemblies: Photoinduced Charge Transfer Interactions", *Advanced Materials*, vol. 17, no. 20, pp. 2458-2463, Oct. 2005.

[21] M. Madou, *Fundamentals of Microfabrication.* New York: CRC Press, 1997, pp. 96-368.

[22] H. Lorenz, M. Despont, N. Fahrni, N. Labianca, P. Vettiger, and P. Renaud, "EPON SU-8 : A low-cost negative resist for MEMS", *Journal of. Micromech. Microeng.*, vol. 7, no. 3, pp. 121-124, Apr. 1997.

[23] W. Kern and C. A. Deckert, *Chemical etching in thin film processes.* New York: Academic Press, 1978, pp. 401-496.

[24] Equipment processes (2006), Alberta NANOFAB, [Online]. Available: http://www.nanofab.ualberta.ca/equipment_process.php

Reproduced with permission of the copyright owner. Further reproduction prohibited without permission.

[25] Process Catalogue (2006), MEMS Exchange, [Online] Available: http://www.mems-exchange.org/catalog/

Reproduced with permission of the copyright owner. Further reproduction prohibited without permission.

APPENDICES

Reproduced with permission of the copyright owner. Further reproduction prohibited without permission.

Matlab Optical Generation Rates

```
% Global Constants
q = 1.6e-19;              % Charge of an electron
h = 6.62e-34;             % Planck's Constant
A = 2e5;                  % Constant for absorption coefficient
c = 3e8;                  % Speed of Light


% Determining the best Material to use by determining the MAX
CUT-OFF
% wavelength. Choices are GaAs, CdS, InP



% bandgap energies
Egcds = 2.42;
Eggaas = 1.43;
Eginp = 1.35;
Egzns =  3.6;
Eggap = 3.4;

%Converting eV to J
wcds = Egcds * q;
wgaas = Eggaas * q;
winp = Eginp * q;
wzns = Egzns * q;
wgap = Eggap * q;

lmaxcds = (h*c)/wcds
lmaxgaas =(h*c)/wgaas
lmaxinp = (h*c)/winp
lmaxzns =(h*c)/wzns
%lmaxgap =(h*c)/wgan
lmax = [lmaxcds lmaxgaas lmaxinp lmaxzns ] .* 1e9

% Visible Light Spectrum
disp('400nm(violet) to 800nm(red)')

% Light Absorbtion

x = 100e-6;         % position in X
y = 100e-6;         % position in Y
```

Reproduced with permission of the copyright owner. Further reproduction prohibited without permission.

```
z = 100e-6;          % position in Z

dx = 10e-6;          % Length in X of Photodetector
dz = 10e-6;          % Length in Z of Photodetector

theta1 = atan((x-dx/2)/y)    % Primary Radiation angle (x-y plane)
theta2 = atan((x+dx/2)/y)    % Secondary Radiation angle (x-y
plane)

deltheta = theta2 - theta1   % Difference in Radiation Angle

phi1 = atan((z-dz/2)/y)    % Primary Radiation angle (y-z plane)
phi2 = atan((z+dz/2)/y)    % Secondary Radiation Angle (y-z plane)

delphi = phi2-phi1

Asph = 4*pi*y^2          % Area of a Sphere

Arcx = y * deltheta        % Arc Length in X
Arcz = y * delphi          % Arc LEngth in Y

Aphoto = Arcx * Arcz       % Sphercial Area of incident photons

Surfphoto = Aphoto/Asph    % Percent Coverage

% We know that there is 10^6 photons released per flash
% This will be the number of photons absorbed into the
% Photodetector.
%
% Assuming that photons are released symetrically over the
% Surface area of the bubble and that absorbtion loss
% into the water is neglected, since the distance to the
% photodetector is small

photonin = 1e5 %Surfphoto *  1e6  % 1e6 is the number of photons
released per
                             % flash of light

% For Optically generated Current gopt is the optical generation
rate
% this is required to determine the amount of Electron Hole
Pairs(EHPs/Area)
% released when photons hit the material. Also assuming that the
material
% is an optically linear medium: Typical Values of neff
(efficiency) range
% from 5% to 30%

neff = 0.05:0.05:0.30;       % Quantum Efficiency
```

Reproduced with permission of the copyright owner. Further reproduction prohibited without permission.

```
lambda = 460e-9;                % Wavelength of blue light
length = 10e-6;
hv =(h*c/lambda)/1.6e-19;       % Energy of the incomming photon
alpha = A*(hv - Egcds);             % absorption coefficient for
CdS
                                % when hv >= Eg, energy of photon
greater
                                % than bandgap energy (based on
Urback's
                                % rule for thin films)

Popt = hv*1.6e-19 * 25000       % Optical Power Intensity of 1
photon

gopt = (alpha * Popt /(dz*dx*hv))*photonin * .3   % optical
generation rate

           % Optically Generated Current
Iopt = (1-exp(-alpha*20e-6))*gopt/hv * Popt
% Responsivity of the photodector

S = neff * q * lambda / (h*c);              % Responsivity

%axis on

%plot(neff,S)
%title('Responsivity')
%xlabel('efficiency')
%ylabel('Responsivity [A/W]')
%figure;
%plot(neff,Iopt)
%title('Current')
%xlabel('efficiency')
%ylabel('Optical Current [A]')
%figure;
%plot(neff,gopt)
%title('optical generation rate')
%xlabel('efficiency')
%ylabel('EHP Generation Rate [EHP/um^2]')
```

Reproduced with permission of the copyright owner. Further reproduction prohibited without permission.

Matlab Capacitive Sensing Model

```
clear;
L=300e-6; % length of the chamber
topx1 = 0;
topx2 = 10e-6;
botx1 = 0;
botx2 = 10e-6;
Arraysizex = 3;
Arraysizey = 3;

% centerpoints for the bubble and other bubble info
circx = 5e-6;
circy = 150e-6;
radius = 5e-6;

% this array calculates all the lines of each plate
% corresponding to each plate

for K=1:Arraysizey,

    for I=1:Arraysizex,
              d(I,K) = sqrt(botx1^2 + L^2);
            if botx1==topx1
               slope1(I,K) = inf;
               intercept1(I,K) = inf;
            else
               slope1(I,K) = (-L)/(botx1-topx1);
               intercept1(I,K) = L - slope1(I,K)*topx1;

            end

            if botx2==topx2
               slope2(I,K) = inf;
               intercept2(I,K) = inf;
            else
               slope2(I,K) = (-L)/(botx2-topx2);
               intercept2(I,K) = L - slope2(I,K)*topx2;
            end

        botx1 = botx1 + 12e-6;
        botx2 = botx2 + 12e-6;

    end
```

Reproduced with permission of the copyright owner. Further reproduction prohibited without permission.

```
    topx1 = topx1 + 12e-6;
    topx2 = topx2 + 12e-6;
    botx1 = 0;
    botx2 = 10e-6;

end


% Minimum distance equation
% d = |ax + by + c| / sqrt(a^2 + b^2)

% Reinitializing counters
botx1 = 0;
botx2 = 10e-6;
topx1 = 0;
topx2 = 10e-6;

for K=1:Arraysizey,

    for I=1:Arraysizex,

        if slope1(I,K) == Inf,
           dist1(I,K) = abs(circx-botx1);
        else
           dist1(I,K) = abs(((-slope1(I,K))*circx+circy-
intercept1(I,K)))/(sqrt(slope1(I,K)^2 + 1^2));
        end

        if slope2(I,K) == Inf,
           dist2(I,K) = abs(circx-botx2);
        else
           dist2(I,K) = abs(((-slope2(I,K))*circx+circy-
intercept2(I,K)))/(sqrt(slope2(I,K)^2 + 1^2));
        end

        botx1 = botx1 + 12e-6;
        botx2 = botx2 + 12e-6;

    end

    topx1 = topx1 + 12e-6;
    topx2 = topx2 + 12e-6;
    botx1 = 0;
    botx2 = 10e-6;

end

% Calculates theta and Effective Area values
```

Reproduced with permission of the copyright owner. Further reproduction prohibited without permission.

```
botx1 = 0;
topx1 = 0;

for K=1:Arraysizey

     for I=1:Arraysizex
         theta(I,K) = abs(atan(((botx1-topx1)/L)*180/pi));
         EA(I,K) = d(I,K).*sin(90-theta(I,K));
         botx1 = botx1 + 12e-6;
    end
    topx1 = topx1 + 12e-6;
    botx1 = 0;
end

% Calculates Distance Between Lines

botx1 = 0;
botx2 = 10e-6;
topx1 = 0;
topx2 = 10e-6;

for K=1:Arraysizey

     for I=1:Arraysizex
         if slope1(I,K) & slope2(I,K) == Inf,
            distlns(I,K) = 10e-6;
         else
             distlns(I,K) = 10e-6 * sin(90-theta(I,K)*pi/180);
         end
     end
    topx1 = topx1 + 12e-6;
    topx2 = topx2 + 12e-6;
    botx1 = 0;
    botx2 = 10e-6;
end

%calculating epsilons and capacitance equations
kwater = 78.5;
kair = 1;
e0 = 8.854e-12;

for K=1:Arraysizey

     for I=1:Arraysizex

         if dist1(I,K) > radius & dist2(I,K) > radius +
distlns(I,K) |...
                 dist2(I,K) > radius & dist1(I,K) > radius +
distlns(I,K),
```

Reproduced with permission of the copyright owner. Further reproduction prohibited without permission.

```
            etotal(I,K) = kwater*e0;
            Totalcap(I,K) = etotal(I,K) * EA(I,K) / d(I,K);

        else if dist1(I,K) < radius,
                Awater(I,K) = abs(dist2(I,K) - radius);
                Aair(I,K) = dist1(I,K)
                Cwater1 = e0*kwater*Awater(I,K)/d(I,K);
                Cwater2 = e0*kwater/ (L-(circy+radius));
                Cwater3 = e0*kwater/(circy - radius);
                Cair = e0*kair(dist1(I,K) + radius);
                Cap1 = 1 / (1/Cwater2 + 1/Cwater3 + 1/Cair);
                Totalcap(I,K) = Cap1 + Cwater1;
            else if dist2(I,K) < radius;
                Awater(I,K) = abs(dist1(I,K) - radius);
                Aair(I,K) = dist2(I,K)
                Cwater1 = e0*kwater*Awater(I,K)/d(I,K);
                Cwater2 = e0*kwater/ (L-(circy+radius));
                Cwater3 = e0*kwater/(circy - radius);
                Cair = e0*kair(dist1(I,K) + radius);
                Cap1 = 1 / (1/Cwater2 + 1/Cwater3 + 1/Cair);
                Totalcap(I,K) = Cap1 + Cwater1;

    end

end
```

Reproduced with permission of the copyright owner. Further reproduction prohibited without permission.

Matlab Bjerknes Forces vs. Buoyancy Forces

```
%Andrew Tam
%Bubble Dynamics Plotting Expansion of a bubble in a Sound
Pressure
%Field with the following parameters

% Driving sound pressure field

f = 20000;                    % Frequency Hz
w = 2*pi*f;                   % rad/sec
t = 0:0.0000001:0.00015;      % Time sec
Pap = 1.4;                    % Drive Pressure Amplidtude atm
Pa = Pap*cos(w*t);            % Drive Pressure Sinusoid
axis on;
plot(t,Pa)
xlabel('time (sec)');
ylabel('Pressure (atm)');

densityp = 1.29;     % Density of Air kg/m^3
P0 = 1.0;            % Ambient Pressure atm
RAdot = real(2/3*((Pa - P0)/densityp).^(1/2)); % Radius Size w/r
to pressure
hold on;
plot(t,RAdot,'k')  % Plots bubble size as a function of time due
to sound pressure

%Forces

rw = 0.15;  % radius of the body of water
r = 0.075   % center of flask
RA = 7e-6;  % Initial Radius
A = pi*RA^2; % Area of Bubble

Pr = 1/r*sin(pi*r/rw)*sin(w*t);
V = 4/3*pi*(50000*RA*RAdot).^3; %Volume of bubble 50000 is a
scaling factor

hold on;
plot(t,V,'r') % Plots Volume vs. Time

Fbuoy = 9.81*(densityp-1)*V; % Buoyancy Forces
Fbjer = -V.*Pr;  % bjerknes forces

figure;
```

Reproduced with permission of the copyright owner. Further reproduction prohibited without permission.

```
subplot(3,1,1)
plot(t,5000*Fbjer) % Plots Bjerkenes Forces 5000 is a scaling
factor
title('Bjerknes Forces');
xlabel('time (sec)');
ylabel('Force (nN');
subplot(3,1,2)
plot(t,100*Fbuoy) % Plots Buoyancy Forces 100 is a scaling factor
title('Buoyancy Forces');
xlabel('time (sec)');
ylabel('Force (nN');
subplot(3,1,3)
plot(t,abs(Pa))
title('Pressure Field');
xlabel('time(sec)')
ylabel('Pressure (atm)')
```

Reproduced with permission of the copyright owner. Further reproduction prohibited without permission.

VITA AUCTORIS

Andrew Tam

2004 – Present	M.A.Sc. Electrical & Computer Engineering, University of Windsor
2000 – 2004	B.A.Sc. Electrical & Computer Engineering, University of Windsor

Reproduced with permission of the copyright owner. Further reproduction prohibited without permission.